Advanced Electronic Materials

ADVANCED ELECTRONIC MATERIALS Open Access

www.advelectronicmat.de

RESEARCH ARTICLE OPEN ACCESS

Precise Tailoring of Charge Transport Characteristics in Zr and Hf Doped Indium Tin Oxide Thin Film Transistors

Marie Isabelle Büschges[1] | Christian Dietz[2] | Vanessa Trouillet[3] | Ann-Christin Dippel[4] | Fernando Igoa Saldaña[4] | Jörg J. Schneider[1]

[1]Fachbereich Chemie, Eduard-Zintl-Institute, Inorganic Chemistry, TU Darmstadt, Darmstadt, Germany | [2]Physics of Surfaces, Institute of Materials Science, TU Darmstadt, Darmstadt, Germany | [3]Institute for Applied Materials (IAM-ESS) and Karlsruhe Nano Micro Facility (KNMFi), Karlsruhe Institute of Technology (KIT), Eggenstein-Leopoldshafen, Germany | [4]Deutsches Elektronen-Synchrotron DESY, Hamburg, Germany

Correspondence: Jörg J. Schneider (joerg.schneider@tu-darmstadt.de)

Received: 13 October 2025 | **Revised:** 5 January 2026 | **Accepted:** 22 January 2026

Keywords: doped ITO | hafnium oxide | metal oxides | semiconductors | thin film transistors | zirconium oxide

ABSTRACT

Zirconium and hafnium doped indium tin oxide (ITO) thin films are fabricated via atomic layer deposition (ALD) at 200°C from trimethylindium, tetrakis(dimethylamido)tin, tetrakis(dimethylamido)zirconium, and tetrakis(diethylamido)hafnium, using water as oxidant. Grazing incidence X-ray total scattering employing synchrotron radiation reveals a highly disordered structure with a short-range order, exhibiting correlation lengths of up to ~13 Å. This is also reflected in high-resolution transmission electron microscopy, revealing an amorphous intermixed state of all constituting components. Increasing amounts of fully coordinated oxygen species with increasing amounts of dopant are evidenced by X-ray photoelectron spectroscopy analysis and attributed to zirconium and hafnium's ability to form strong oxygen bonds, and thereby suppressing the formation of oxygen vacancies. The Zr- and Hf-doped ITO thin films are integrated into thin-film transistor (TFT) devices to evaluate their suitability as semiconducting material. The electrical measurements reveal saturation mobilities (μ_{sat}) of 1.92–9.81 $cm^2\ V^{-1}\ s^{-1}$, with high current on/off ratios (I_{On}/I_{Off}) of 10^6–10^8. This study demonstrates the subtle influence of small amounts of Zr and Hf on TFT performance. This proves the ability to control the electrical behavior of TFT devices by controlled incorporation of dopants like Zr and Hf into their active channel layer.

1 | Introduction

The significance of thin-film transistors (TFTs) has been well-established over the past several decades. TFTs have found application in switching and driving devices in large OLED TV displays [1, 2], sensors [3] and thin film solar cells [4], to only name a few. Transparent semiconducting oxides are of significant interest due to their numerous distinctive characteristics, including high optical transparency, high mobility, low off-current, and low processing temperature [5–7]. Following the initial report on amorphous indium-gallium-zinc-oxide (a-IGZO) [5] as a semiconductor for the active channel in TFT devices, there has been a considerable increase in the research interest concerning amorphous oxide semiconductor (AOS) based TFT channel materials. Due to its exceptional characteristics, research has been predominantly focused on IGZO [8]. However, other materials have also demonstrated their potential as active channel material. Numerous studies have reported the fabrication of TFTs with multicomponent materials that exhibit desirable properties. These include In-Zn-O (IZO) [9, 10], In-Zn-Sn-O (IZTO) [11, 12], Zn-Sn-O (ZTO) [13, 14], and Al-Zn-Sn-O (AZTO) [15], exhibiting mobilities between 4.5 and 41 $cm^2\ V^{-1}\ s^{-1}$ [9, 12].

Substantial research has been dedicated to enhancing the electrical characteristics, particularly the mobility, of AOS-based TFTs. A number of possibilities have been reported, including increasing the indium ratio of a multicomponent material [16, 17] or controlling the oxygen vacancy concentration [8, 18]. An increased indium ratio leads to an increased charge carrier concentration, consequently increasing the off-current and resulting in poor switching behavior of the respective TFT [17, 19]. Typically, the concentration of oxygen vacancies is regulated by the introduction of an ion that forms a strong oxygen bond (M—O), and is thereby able to suppress the formation of these vacancies. Gallium is frequently selected for this purpose, though alternative materials, including hafnium [20, 21], zirconium [22], yttrium [23], magnesium [24, 25], and aluminum [26], have been reported to demonstrate comparable effects when incorporated into the semiconducting film [8]. The incorporation of these ions has also been reported to enhance the stability of the resulting TFTs by passivating the trap density at the dielectric/semiconductor interface [20, 22, 23]. However, a balance must be established between the suppression of oxygen vacancies and the enhancement of the stability, as both are crucial for optimal TFT device operation. Therefore, it is imperative to carefully modulate the cation and oxygen ratio [27].

The composition of the semiconductor is primarily controlled by the processing technique. Conventional methods such as physical vapor deposition or sputtering have been shown to exhibit certain disadvantages, including high processing temperatures, inhomogeneous film thickness distribution, and constrained compositional control [27]. Atomic layer deposition (ALD) is a fabrication method that addresses the aforementioned challenges and allows for the straightforward deposition of multicomponent thin films. ALD allows for the fabrication of thin films exhibiting high quality and homogeneity, with precise thickness and compositional control at growth temperatures below 350°C [28]. The ALD process is predominantly characterized by sequential surface reactions. The metal precursor and co-reactant are successively brought into contact with the substrate on which the thin film is deposited, separated by an inert gas purging step [29]. These surface reactions are self-limiting in nature, as the precursor reaches a state of self-saturation once all active surface sites are occupied [27]. Consequently, a maximum of one monolayer is deposited per reaction cycle, with the growth rate per cycle (GPC) generally being less than one Ångstrom per cycle [28]. The layer-by-layer deposition process allows for precise thickness control at the angstrom level [28]. Furthermore, a supercycle approach enables the modulation and variation of the composition and cation distribution in multicomponent materials through the successive deposition of multiple binary ALD cycles. In the field of semiconductor materials, compositional control is of particular significance due to its substantial impact on the electrical characteristics of the resulting TFT devices [27]. By varying the ratio of indium, gallium, and zinc in IGZO thin films, they were able to obtain mobility values ranging from 30.24–81.6 $cm^2\ V^{-1}\ s^{-1}$, with a subthreshold swing between 0.09–0.5 V dec^{-1}, and an on/off ratio between 1×10^8–3.5×10^8 [30]. The advantages of ALD, including homogeneous film growth over large areas, precise thickness and compositional control, and low processing temperatures, have established this process as a next-generation deposition technique for the fabrication of high-mobility and high-stability semiconducting thin films for TFT applications.

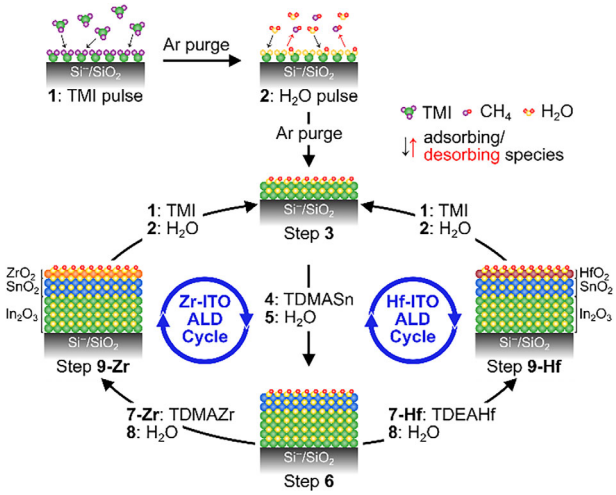

FIGURE 1 | Schematic of the ALD process for Zr- and Hf-doped ITO thin films. The sequence is shown in detail for indium oxide: (1) TMI is pulsed into the reaction chamber, where it reacts with OH-groups of the substrate; (2) water is introduced and oxidizes surface groups, forming hydroxyl groups and CH_4, followed by an argon purge restoring the conditions for the next deposition; repetition of (1) and (2) is denoted as step 3. From TDMASn (4) and H_2O (5), tin oxide is deposited (step 6), while TDEAHf (7-Hf) or TDMAZr (7-Zr) and H_2O (8) are used to deposit hafnium- or zirconium oxide (step 9-Hf or 9-Zr). Repetition of a supercycle increases the film's thickness, and alternating the supercycle leads to a mixed Hf/Zr or Zr/Hf heterostack.

In this study, we investigated the doping of indium tin oxide (ITO) thin films with zirconium and hafnium oxide. Both Zr and Hf are elements with a high tendency to form strong oxygen bonds. The fabrication of the thin films by ALD enables precise control over the compositional ratios and film thicknesses. Following a thorough material characterization process, the thin films were integrated into TFT devices to ascertain the impact of the doped ions on the device's electrical performance. Our findings enabled the fabrication of TFT devices incorporating both Zr and Hf, showing a distinct influence on the TFT performance parameters.

2 | Results and Discussion

Figure 1 provides a schematic representation of the employed ALD deposition process. The initial step (**1**) in the process involves the exposure of the substrate to the metal precursor (TMI: trimethylindium). The reaction of surface OH-groups with precursor molecules leads to the formation of surface bonds, accompanied by the release of volatile by-products. Following a designated exposition time, an argon purge is employed to remove excess precursor and by-products. Subsequently, water is introduced as oxidant into the reaction chamber (**2**), where it reacts with the organic groups of the previously deposited metal precursor molecules, forming hydroxyl groups on the films' surface, thereby producing by-products. Another argon purge is then employed to remove these molecules from the reaction chamber, thus restoring the environment for a subsequent

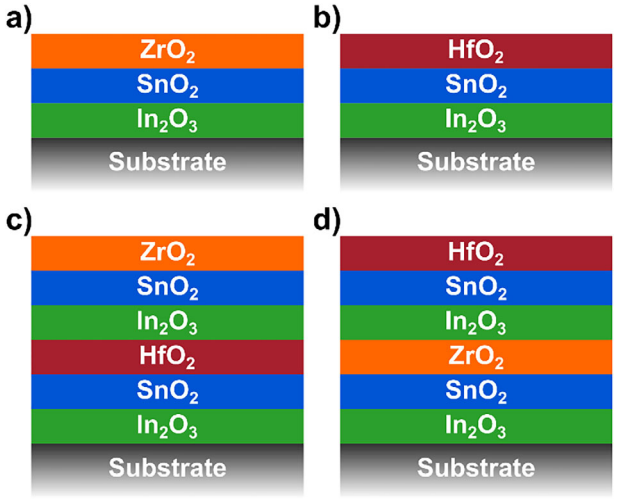

FIGURE 2 | Stacking sequence of the metal oxides, shown in one supercycle for (a) Zr-ITO, (b) Hf-ITO, (c) Hf/Zr-ITO, and (d) Zr/Hf-ITO. For Hf/Zr-ITO, the Zr-ITO supercycle is stacked on top of the Hf-ITO supercycle, and for Zr/Hf-ITO the order is inverted.

reaction cycle. Repetition of the preceding steps (**1** and **2**) enables the modulation of the layer thickness of the individual oxide (Step **3**). The deposition of doped ITO thin films is achieved through the utilization of trimethylindium (TMI) for indium oxide, tetrakis(dimethylamido)tin(IV) (TDMASn) for tin oxide, tetrakis(dimethylamido)zirconium(IV) (TDMAZr) for zirconium oxide, and tetrakis(diethylamido)hafnium(IV) (TDEAHf) for hafnium oxide, respectively. Water is employed as the oxidant in each deposition process. For the Zr- and Hf-doped ITO thin films under investigation, the deposition of indium oxide is conducted in 26 cycles, succeeded by 15 cycles of tin oxide (**4**, **5**, Step **6**). Doping is achieved by the subsequent deposition of 1–3 cycles of hafnium (**7-Hf**, **8**, Step **9-Hf**) or zirconium oxide (**7-Zr**, **8**, Step **9-Zr**), respectively. The thin films doped with both Zr and Hf were deposited employing two cycles of hafnium- and two cycles of zirconium oxide, respectively.

As illustrated in Figure 1, the Zr-ITO ALD cycle and the Hf-ITO ALD cycle are representative of the deposition of a single supercycle of the heterostack. The supercycle is repeated until the desired overall film thickness is attained. In the case of the Zr- and Hf-doped ITO thin films, the supercycle is repeated eight (8) times in order to obtain a film thickness of approximately 8 nm. The deposition of the thin films doped with both Zr and Hf is achieved through the alternation of the Zr-ITO and Hf-ITO supercycles. For instance, the process of the Zr/Hf-ITO deposition is initiated by the Zr-ITO supercycle, which is subsequently succeeded by the Hf-ITO supercycle. For the Hf/Zr-ITO deposition, the sequence of the supercycles is reversed. In order to achieve an approximately equivalent overall film thickness, the process is repeated a total of four (4) times, with each repetition unit consisting of one Hf-ITO supercycle and one Zr-ITO supercycle. Figure 2 provides a schematic representation of the employed stacking sequence of a single supercycle. An overview of the composition of each sample is given in Table 1.

The high-resolution transmission electron microscopy (HRTEM) image of a cross-section of the thin film Hf-ITO 2, prepared by

TABLE 1 | Compositional overview for the Zr-ITO, Hf-ITO, and mixed Hf/Zr- and Zr/Hf-ITO thin films.

Sample	In_2O_3	SnO_2	ZrO_2	HfO_2	Super cycles
Zr-ITO 1	26	15	1	—	8
Zr-ITO 2	26	15	2	—	8
Zr-ITO 3	26	15	3	—	8
Hf-ITO 1	26	15	—	1	8
Hf-ITO 2	26	15	—	2	8
Hf-ITO 3	26	15	—	3	8
Hf/Zr-ITO	26	15	2	2	4
Zr/Hf-ITO	26	15	2	2	4

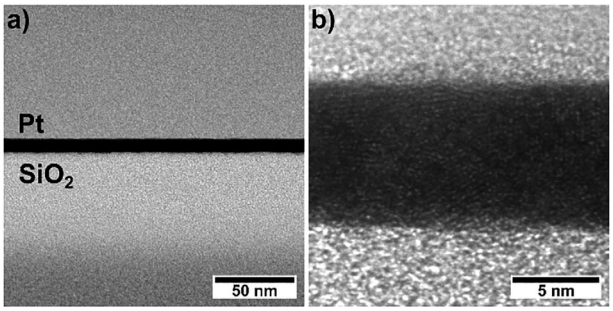

FIGURE 3 | HRTEM cross-section of the thin film Hf-ITO 2. The highly conformal layer thickness is observable in (a), while (b) reveals an amorphous nature of the thin film (but see also discussion below).

focused ion beam (FIB) is depicted in Figure 3 (for Zr-ITO 2 and Zr/Hf-ITO see Figure S1). The HRTEM image (Figure 3a) reveals a uniform film thickness of ~8 nm over a substantial range, exhibiting a high degree of homogeneity, proving the conformality of the deposition process. The amorphous nature of the thin film is revealed by the high-resolution image in Figure 3b). It is notable that the presence of isolated and obviously crystalline areas in the one nm regime or even below reflecting ordered structures can be detected by visual inspection under high resolution on a computer screen. This observation is in full accord with grazing incidence X-ray total scattering (GI-XTS) studies, which allow to detect nearest atomic ordering with a correlation length of ~10–13 Å (see below). The individual layers of the single oxides have undergone interdiffusion, resulting in the formation of a single homogeneous layer. The observation of interdiffusion is also supported by the thermal post annealing process of the thin films at 300°. A similar observation was made in our earlier study on magnesium-doped ITO thin films [25]. The presented results are consistent for all investigated samples (Hf-ITO 2, Zr-ITO 2, and Zr/Hf-ITO).

X-ray photoelectron spectroscopy (XPS) was employed to obtain further insight into the composition of the doped ITO heterostacks, with a particular focus on the individual concentrations of Zr and Hf dopant elements. The O 1*s* core level (Figure 4a) is deconvoluted into two peaks situated at binding energies (BE) of 530 and 531.6 eV. While the former can be attributed to fully coordinated oxygen species (M—O) associated with metal oxides [31–34], the latter can be assigned to metal hydroxide species

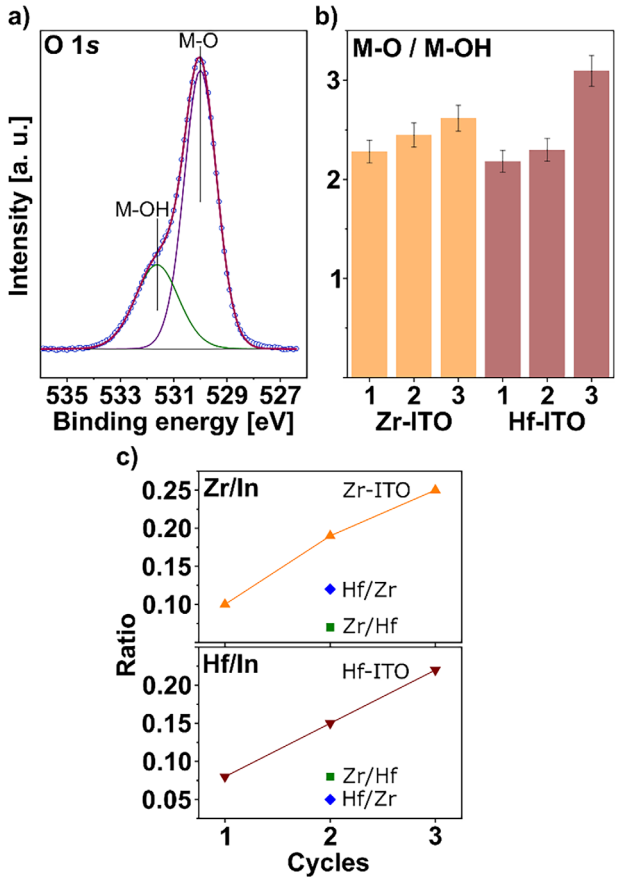

FIGURE 4 | (a) O 1*s* core level spectra of the Hf/Zr-ITO thin film, deconvoluted into two peaks. All spectra are referenced to the C 1*s* peak at 285 eV. In (b), the ratio of M—O (530 eV) to M—OH (531.6 eV) for the Zr-ITO (orange) and Hf-ITO (red) thin films is depicted, while (c) illustrates the ratios Zr/In (top) and Hf/In (bottom) calculated from the Zr 3*d*, Hf 4*d*, and In 3*d* core levels (Table S2) for all doped ITO thin film.

(M—OH) present within the thin film and on the samples' surface [31, 32, 34]. As the concentration of Zr and Hf increases in the thin films, the amount of the fully oxidized M—O species also increases. For Zr-ITO, the amount of M—O tendentially increases from 37.6 to 39.5 at%, and for Hf-ITO, it increases from 37.3 to 39.9 at%, respectively. Simultaneously, the contribution of M—OH decreases with increasing amounts of Zr and Hf content (Table S1). The concurrent increase of M—O (530 eV) and decrease of M—OH (531.6 eV) of the Zr-ITO, Hf-ITO, and mixed Hf/Zr- and Zr/Hf-ITO thin films is illustrated in Figure 4b as the ratio M-O/M—OH. The increase in M—O species can be attributed to the bond dissociation energies (BDE) of the metal oxides that comprise the thin films. A comparison of the M—O bonding properties of zirconium (766.1 ± 10.6 kJ mol^{-1}) [35, 36], hafnium (801 ± 13 kJ mol^{-1}) [35, 36], indium (346 ± 30 kJ mol^{-1}) [35, 36], and tin (528 kJ mol^{-1}) [35, 36] reveals that the former two tend to form stronger oxygen bonds. Consequently, an increase in the amount of these high BDE elements results in more fully coordinated oxygen species and therefore to fewer oxygen vacancies.

The quantitative analysis of the Zr 3*d* and Hf 4*d* core levels confirms increasing concentrations of Zr and Hf in the thin films with increasing numbers of deposited TDMAZr and TDEAHf cycles, respectively. The concentration of Zr increases from 2 to 5 at% for Zr-ITO 1 to Zr-ITO 3, while the Hf concentration increases from 1.6 to 4 at% for Hf-ITO 1 to Hf-ITO 3 (Table S2). Concurrently, the amount of indium remains constant at approximately 20 at% for Zr-ITO 1-3 but exhibits a slight decrease from 20.7 at% for Hf-ITO 1 to 18.5 at% for Hf-ITO 3 (Table S2). The observed trend can also be expressed by the ratios of Zr/In and Hf/In, which exhibit an increase from 0.10 (Zr-ITO 1) to 0.25 (Zr-ITO 3) and 0.08 (Hf-ITO 1) to 0.22 (Hf-ITO 3) (Figure 4c). In the case of Zr/Hf-ITO, the amounts of zirconium and hafnium are similar with 1.5 and 1.7 at.%, respectively. By contrast, for Hf/Zr-ITO these values differ to a greater extent, with 2.4 at% for zirconium and 1 at% for hafnium. Consequently, the ratios Zr/In and Hf/In exhibit divergent values for the mixed Hf/Zr- and Zr/Hf-ITO samples, with 0.12 and 0.05 for Hf/Zr-ITO and 0.07 and 0.08 for Zr/Hf-ITO, respectively (Figure 4c). However, both mixed Hf/Zr- and Zr/Hf-ITO samples exhibit nearly constant values for indium and tin with ~20 and ~6 at%, respectively (Table S2).

The total carbon content of all samples is found to be constant at ~15.5 at%, suggesting that the presence of carbon is limited to the surface and subsurface of the films due to exposure to the atmosphere during handling (Table S1) [37, 38]. A study on the effect of the sample storage environment on the adventitious carbon content on metal oxides gives further support of the presence of similar carbon contents on the films' surface and comparable carbon species [39]. For the films studied herein, the C 1*s* core level (Figure S2e) shows three peaks which can be assigned to —C—C and —C—H groups at 285 eV, stemming from hydrocarbon contamination [40], —C—O groups at 286.4 eV, and carboxylic groups (O—C═O) at 289 eV [31, 41]. The three components have contributions for all samples of ~11 at% for —C—C/—C—H groups, ~3 at% for —C—O groups, and ~2.5 at% for O—C═O groups, which is in agreement with the range of concentrations found for similar sample treatment under ambient conditions [39]. The core level spectra for zirconium (Zr 3*d*), hafnium (Hf 4*d*), indium (In 3*d*), and tin (Sn 3*d*), as well as the In MNN-Auger line and the valence band (VB) region are depicted in Figure S2. The binding energies (BE) of the Zr 3*d* and Hf 4*d* core levels (Figure S2a,b) are consistent with previously reported values, with Zr $3d_{5/2}$ at 182.1 eV with a spin orbital split (SOS) of 2.4 eV and Hf $4d_{5/2}$ at 213.2 eV with a SOS of 10.7 eV [42, 43]. Both core levels exhibit no significant BE shift with increasing amounts of Zr or Hf in the thin films. The Hf 4*d* core level was selected for the quantitative analysis due to the overlap between the Hf 4*f* and the In 4*d* core level (Figure S2f), introducing some uncertainty toward this point [44, 45]. The presence of In_2O_3 is confirmed by the In 3*d* doublet with In $3d_{5/2}$ at 444.6 eV and the In MNN-Auger line (Figure S2c,g), which are in agreement with values reported previously [33, 46]. The Sn 3*d* doublet with Sn $3d_{5/2}$ at 486.6 eV, in addition to the valence band maximum (VBM) at ~4.3 eV (Figure S2d,h) indicates the presence of Sn(IV), in accord with previous values [47, 48].

The high optical transparency of the different heterostacks exhibits slight variability, with 89% for Zr-ITO, 92% for Hf-ITO, and 93% for the mixed Hf/Zr- and Zr/Hf-ITO thin films (Figure 5a). The band gaps of the heterostack structures were determined by Tauc plot analysis (Figure 5b) [49].

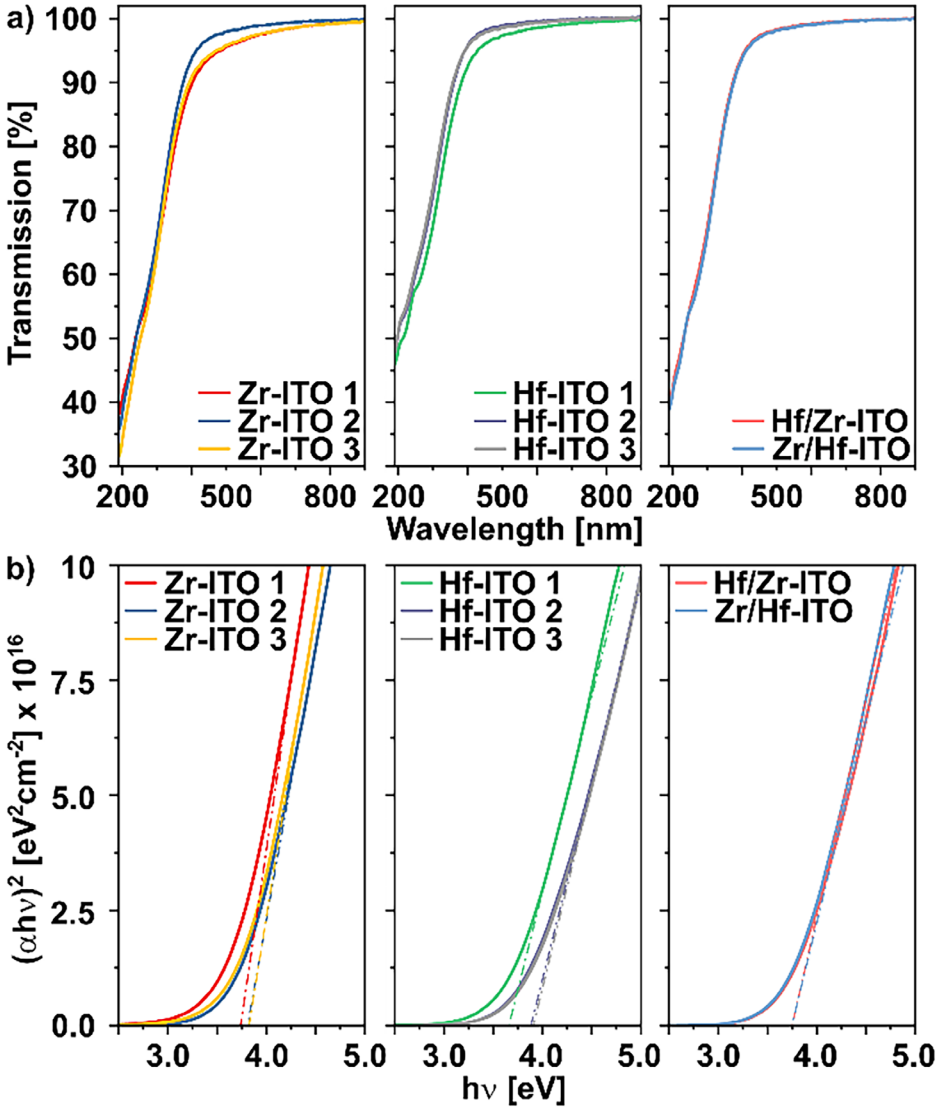

FIGURE 5 | (a) Transmission spectra and (b) Tauc plots of the doped thin films: Zr-ITO left, Hf-ITO middle, mixed Hf/Zr- and Zr/Hf-ITO right.

As evidenced by the Tauc plots in Figure 5b, the thin films with a single cycle of Zr or Hf (Zr-ITO 1 and Hf-ITO 1) exhibit only a minor deviation in the curve progression when compared to the samples with two or three layers. This observation is also reflected by the separation of the respective band gap values for both Zr-ITO and Hf-ITO (Table 2). However, the investigation revealed a modest broadening of the optical band gap in both Zr-ITO and Hf-ITO thin films with increasing amounts of Zr or Hf, respectively. This effect can be anticipated, as zirconium oxide (5–6.2 eV) [50, 51] and hafnium oxide (5.5–5.8 eV) [52, 53] possess larger band gaps in comparison to indium oxide (3.6–3.7 eV) [54] and tin oxide (3.6 eV) [55]. Therefore, the broadening of the optical band gap is solely attributed to the compositional changes of the thin films. In our previous studies on Mg-doped ITO [25] and Al-doped ITO [26], we observed a comparable phenomenon. Similar observations have been reported for other systems, including magnesium-doped zinc oxide [56] or magnesium-doped aluminum zinc oxide [57]. Concurrently, both mixed Hf/Zr- and Zr/Hf-ITO thin films demonstrate nearly identical curve progressions and thus possess an identical band gap value of 3.75 eV.

TABLE 2 | Band gaps calculated from the Tauc plots and corresponding film thicknesses for Zr-ITO 1–3, Hf-ITO 1–3, and mixed Hf/Zr- and Zr/Hf-ITO.

Sample	Band gap (eV)	Thickness (nm)
Zr-ITO 1	3.74	7.59 ± 0.13
Zr-ITO 2	3.81	8.46 ± 0.04
Zr-ITO 3	3.82	8.88 ± 0.06
Hf-ITO 1	3.66	8.06 ± 0.03
Hf-ITO 2	3.88	8.19 ± 0.22
Hf-ITO 3	3.91	7.97 ± 0.13
Hf/Zr-ITO	3.75	8.78 ± 0.04
Zr/Hf-ITO	3.75	8.87 ± 0.03

Grazing incidence X-ray total scattering (GI-XTS) employing synchrotron radiation is used to gain further insight into the

structure of the Zr-ITO and Hf-ITO thin films. Consequently, heterostacks with two, four, and six ALD cycles of Zr and Hf are fabricated to enable more precise evaluation of the impact of the doped materials on the structure. Pair distribution function (PDF) analysis is employed to study the atomic short-range order of the different metal oxides. The obtained PDF data of the Zr-ITO and Hf-ITO thin films are depicted in Figure 6, along with reference data for SnO_2 [58], In_2O_3 [59], and monoclinic ZrO_2 [60] and HfO_2 [61], as well as two different compositions of indium tin oxide, $In_4Sn_3O_{12}$ [62] and $In_{1.88}Sn_{0.12}O_3$ [63]. (Crystallographic data of all references can be found in Table S3).

The PDFs of both Zr-ITO and Hf-ITO thin films show a disordered structure, exhibiting correlation lengths of ~13 Å for Zr-ITO and of ~10 Å for Hf-ITO, respectively (Figure 6a). In the low-r region, between 1.85–4.75 Å, three distinct peaks are observed at ~2.1, ~3.4, and ~3.7 Å (Figure 6b,c), while lower and broader peaks are observable at interatomic distances greater than 5 Å (Figure 6a). Typically, in metal oxides, the shortest correlation length (here ~2.1 Å) is ascribed to nearest-neighbor metal–oxygen bonds, while the next-nearest-neighbor metal–metal interatomic distances give rise to a larger peak at slightly higher r (here ~3.4 Å) [64]. This assertion is validated through comparison with PDFs of reported crystalline reference structures for ITO and the pure metal oxides of indium, tin, hafnium, and zirconium (Figure 6b,c). With the exception of SnO_2, the considered reference phases yield PDFs that look rather similar in the low r region representing the short-range order, although they exhibit different crystal structures and coordinations in addition to different compositions and stoichiometries. The PDF of the trigonal ITO-reference, $In_4Sn_3O_{12}$ (space group $R\bar{3}$) [62], displays distinct peaks at interatomic distances of 2.1, 3.45, and 3.9 Å, which can be correlated to metal–oxygen bonds in the former case and metal–metal distances for the two latter. The cubic ITO-reference, $In_{1.88}Sn_{0.12}O_3$ (space group $Ia\bar{3}$) [63], exhibits analogous characteristics. In this structure, the nearest neighbor M—O bond length is at 2.1 Å, the metal–metal next-nearest-neighbor distance is ~3.4 Å, and the correlation length of ~3.8 Å can be attributed to mixed longer distances. These observations are consistent with monoclinic ZrO_2 and HfO_2 references [60, 61]. In addition, the less intense signals between 2.6–2.9 Å can be attributed to O–O distances [65]. By comparison, tetragonal SnO_2 (space group $P4_2/mnm$) [58] exhibits a slightly shorter metal–oxygen bond length of ~2.05 Å. In this structure, SnO_6 octahedra are connected both via their edges and their corners, leading to metal–metal distances of 3.2 and 3.7 Å, respectively. As the corner-sharing geometry dominates, the PDF peak at 3.7 Å is about four times as high as the peak at 3.2 Å.

For the two sets with varying Hf and Zr contents, the PDFs of the Zr-ITO and Hf-ITO samples show notable similarities on the short-range order scale as illustrated in Figure 6b,c. While the peak positions shift slightly within the data series, a significant shift in the height ratio of the two peaks at ~3.4 and ~3.7 Å is evident with increasing amounts of Zr and Hf, respectively. When looking at this peak height ratio, it can be argued that for samples with low concentrations of Zr and Hf, the local structure resembles that of $In_{1.88}Sn_{0.12}O_3$ [63] and shifts toward a local structure more similar to that of $In_4Sn_3O_{12}$ [62] with increasing amounts of Zr and Hf. A comparison of the two ITO references reveals differences in both their crystal symmetry and coordination geometries. In the cubic $In_{1.88}Sn_{0.12}O_3$ [63], the cations In^{3+} and Sn^{4+} are surrounded by six oxygen atoms and two vacant anion sites, exhibiting a geometry resembling a distorted cube [63]. In the trigonal $In_4Sn_3O_{12}$ [62], the cations demonstrate two different coordination geometries. Sn^{4+} cations are coordinated in a trigonally compressed octahedron by six oxygen anions,

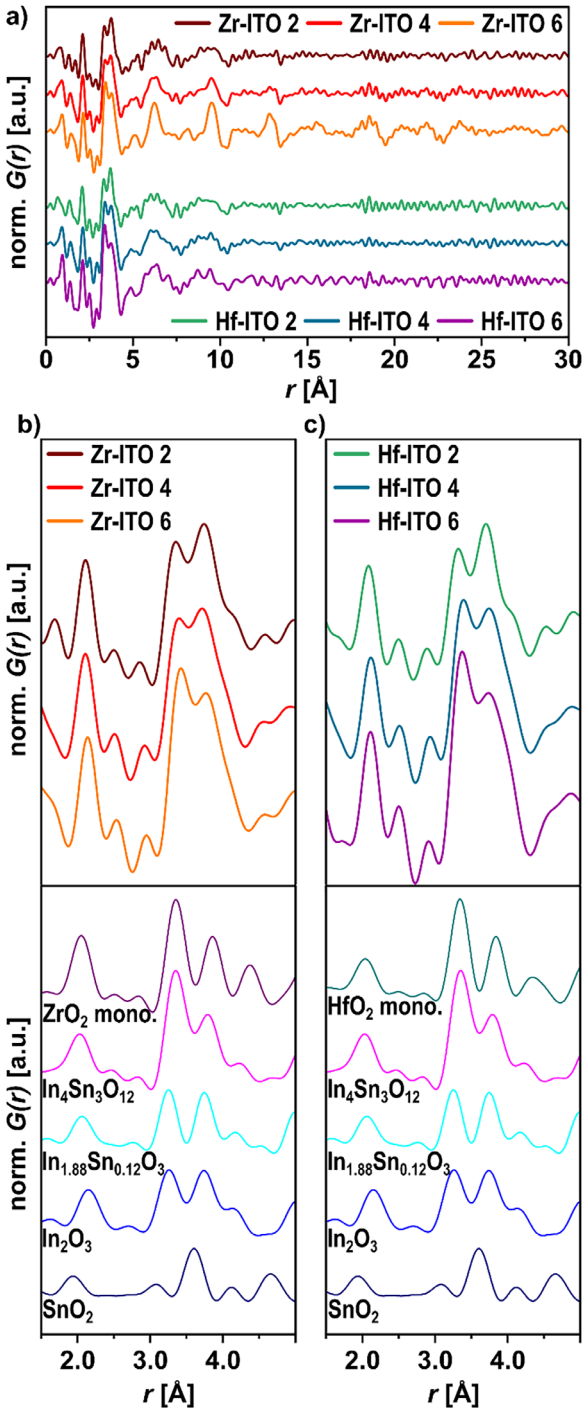

FIGURE 6 | (a) Full r range (0–30 Å) of the normalized PDFs obtained for the Zr-ITO and Hf-ITO thin films. In (b) the PDFs of the Zr-ITO samples (Zr-ITO 2, Zr-ITO 4, Zr-ITO 6) and in (c) the PDFs of the Hf-ITO samples (Hf-ITO 2, Hf-ITO 4, Hf-ITO 6) are depicted along with calculated reference PDFs of monoclinic ZrO_2 [60] or HfO_2 [61], $In_4Sn_3O_{12}$ [62], $In_{1.88}Sn_{0.12}O_3$ [63], In_2O_3 [59], and SnO_2 [58].

while the In^{3+}/Sn^{4+} cations are surrounded by seven oxygen anions, resulting in a highly distorted cube geometry with one corner missing [62]. The described coordination polyhedra for both ITO references are depicted elsewhere [25]. However, this sole presence of the $In_{1.88}Sn_{0.12}O_3$ in the Hf-ITO 2 and Zr-ITO 2 samples does not account for the dominance of the peak at ~3.7 Å over the peak at ~3.4 Å when the Hf and Zr contents are low. Here, a comparison with the calculated PDF of SnO_2 may suggest that these samples contain a certain fraction of pure SnO_2 which adds to the peak height at ~3.7 Å representing corner-sharing SnO_6 octahedra. This hypothesis is supported by the slight peak shift toward lower *r* for the shortest M—O bonds as an overlap of 2.1 Å of the two ITO reference phases and 2.05 Å for the SnO_2 reference phase. In principle, the presence of pure In_2O_3 next to SnO_2 may be taken into account. In cubic In_2O_3 (space group $I2_13$) [59], the first three correlation lengths are ~2.3, 3.4, and 3.9 Å and thus sufficiently close to the observed interatomic distances in the experimental data, though not as good an overall match as the ITO phases. However, it was not possible to precisely reproduce the experimental data by linear combinations of SnO_2 with either In_2O_3 or $In_{1.88}Sn_{0.12}O_3$ (Figure S3). While the peak ratio between 3 and 4 Å matches rather well for $x = 0.15$ in $(1-x)$ $In_2O_3 + x\ SnO_2$ and $x = 0.25$ in $(1-x)$ $In_{1.88}Sn_{0.12}O_3 + x\ SnO_2$, the peak stemming from the nearest-neighbor M—O bonds at ~2.1 Å is narrower in the experimental PDFs. Consequently, the data suggest that the disordered samples are mostly single-phase with different octahedral coordination compared with the crystalline ITO counterparts with for example, more corner-sharing regular SnO_6 octahedra or more of the distorted octahedral motifs with interatomic distances of ~3.7 Å.

It is noteworthy that the ZrO_2 and HfO_2 reference PDFs comprise two peaks in the range between 3 and 4 Å at nearly the same positions as the two ITO reference phases, but with an intermediate peak height ratio. For the samples with the highest Zr and Hf contents, a shoulder on the right side of the peak at ~3.7 Å is visible that matches well with the M–M and M–O distances of ~3.9 Å present in the monoclinic hafnia and zirconia phases. Therefore, the occurrence of the shoulder feature in combination with the shift in peak height ratio could possibly be indicative of the presence of HfO_2 and ZrO_2 layers within the layered stack. Nevertheless, the fact that the ITO and In_2O_3 references exhibit correlation lengths of ~3.9 Å as well, it is not possible to unambiguously distinguish the emergence of HfO_2/ZrO_2 from the occurrence of octahedral coordination more similar to crystalline ITO and In_2O_3.

For each structure, an area of $1 \times 1\ \mu m^2$ was scanned in AFM tapping mode and is depicted in Figure 7. The Hf-ITO thin film exhibits significantly lower surface roughness than the Zr-ITO thin film, with R_{RMS} values of 0.354 and 0.719 nm, respectively. Additionally, both mixed Hf/Zr- and Zr/Hf-ITO thin films show a significant difference in R_{RMS} values with 0.370 and 0.639 nm, respectively. The findings suggest that zirconium exerts a more pronounced influence on the roughness of the thin film when deposited first in the heterostack, while hafnium appears to have a mitigating effect on the overall film roughness. Therefore, it can be deduced that the cumulative effect of the entire stack on the surface roughness is significantly more pronounced than the individual impact of the last deposited material. The surface roughness of all investigated thin films is in accordance with previously reported R_{RMS} values for ALD deposited thin films and appears rather smooth overall [50, 66, 67].

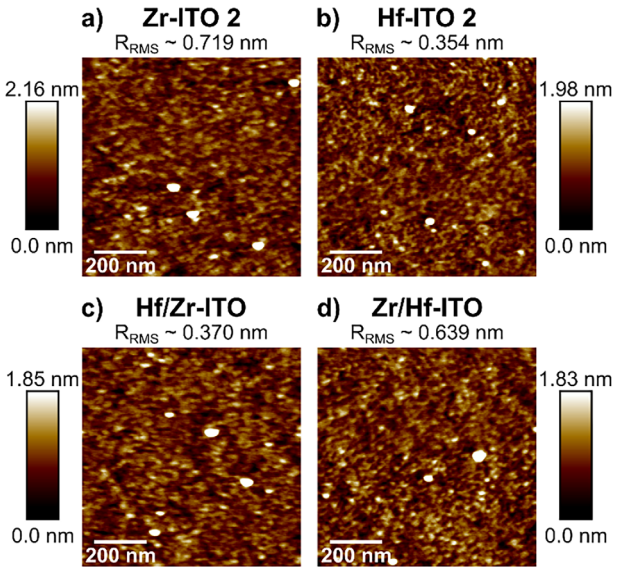

FIGURE 7 | AFM topography images of the heterostructured thin films (a) Zr-ITO 2, (b) Hf-ITO 2, (c) Hf/Zr-ITO, and (d) Zr/Hf-ITO and their corresponding root-mean-square roughness (R_{RMS}) values.

2.1 | Evaluation and Comparison of Hf- and Zr-Doped ITO Thin Films Integrated Into TFT Devices

The evaluation of the doped ITO thin films as a semiconducting layer, and the study of the influence of zirconium- and hafnium oxide on the semiconducting properties, were conducted by integrating the heterostacks into thin film transistor (TFT) devices with a bottom-gate-bottom-contact (BGBC) geometry. Following the deposition process and post-deposition annealing at 350°C, the electrical characterization was performed as current–voltage (IV) measurements. Key performance parameters such as saturation mobility (μ_{sat}), threshold voltage (V_{th}), on-voltage (V_{On}), on/off-ratio (I_{On}/I_{Off}), and subthreshold swing (*SS*) were extracted from the respective transfer characteristics. The collective transfer characteristics of all investigated TFTs are depicted in Figure 8a. To enhance clarity, the transfer characteristics of Zr-ITO, Hf-ITO, and the mixed Hf/Zr- and Zr/Hf-ITO TFTs are shown separately in Figure 8b–d). The extracted performance parameters are summarized in Table 3.

The investigation revealed that both Zr-ITO and Hf-ITO thin films exhibit a decline in mobility with an increasing amount of oxide dopant (either zirconium- or hafnium oxide). The mobility (μ_{sat}) values for Zr-ITO demonstrate a substantial decline, commencing at 8.76 $cm^2\ V^{-1}\ s^{-1}$ for Zr-ITO 1 and decreasing to 1.92 $cm^2\ V^{-1}\ s^{-1}$ for Zr-ITO 3. A less pronounced decrease is observed for Hf-ITO, with mobility values starting at 9.81 $cm^2\ V^{-1}\ s^{-1}$ for Hf-ITO 1 and decreasing to 3.65 $cm^2\ V^{-1}\ s^{-1}$ for Hf-ITO 3. Concurrently, as the quantity of Zr and Hf increases, the on-voltage V_{On} and threshold voltage V_{th} increase simultaneously, for both Zr-ITO and Hf-ITO. The subtle shift of V_{On} can be observed in Figure 8b,c for Zr-ITO and Hf-ITO, respectively.

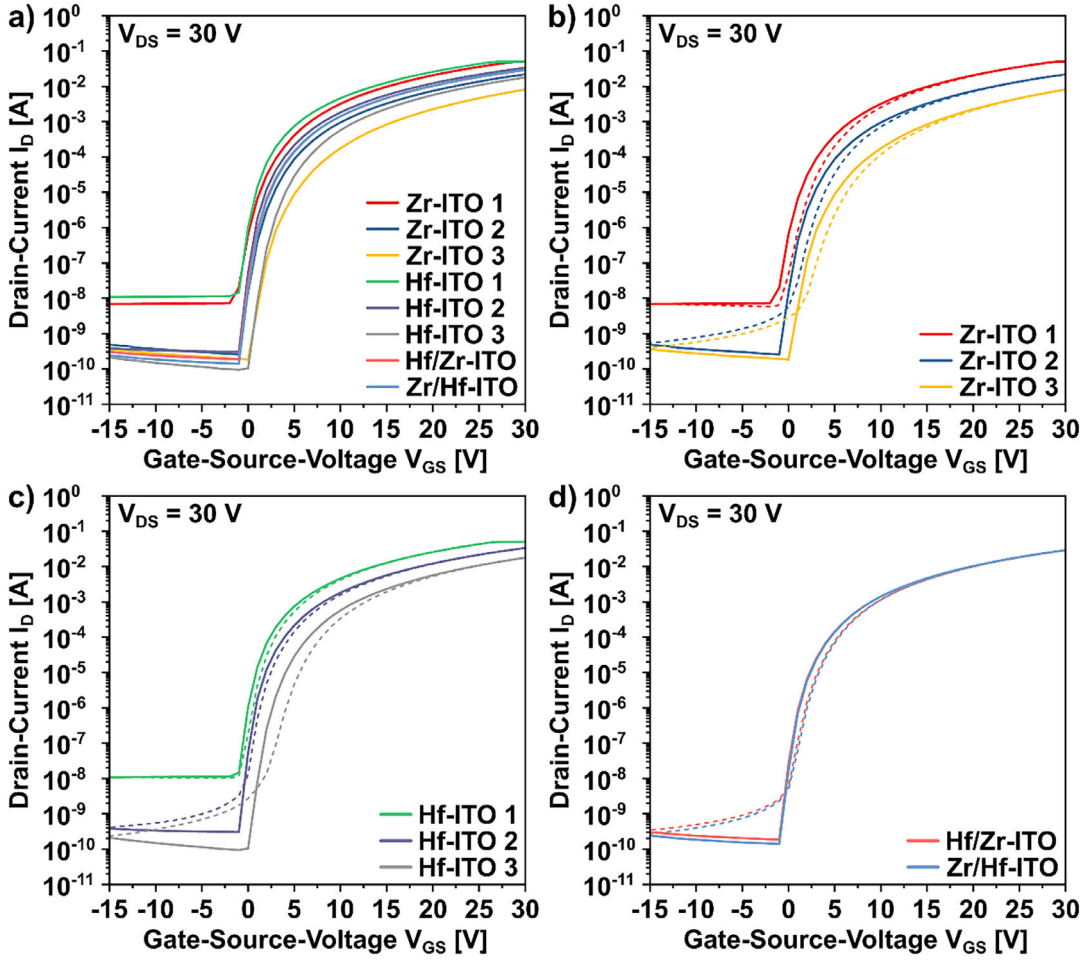

FIGURE 8 | Collective transfer characteristics of all doped ITO thin films are shown in (a), while (b–d) separately depict the transfer characteristics for Zr-ITO, Hf-ITO, and the mixed Hf/Zr- and Zr/Hf-ITO thin films, respectively. Solid lines represent the forward sweep, while dashed lines denote the backward sweep of the measurement. For Hf-ITO 1, the compliance limit of 0.05 A was reached.

TABLE 3 | TFT performance parameters and trap densities including standard deviations of the doped ITO heterostructure TFT devices.

Sample	Mobility, μ_{sat} ($cm^2\ V^{-1}\ s^{-1}$)	On-voltage, V_{On} (V)	Threshold voltage, V_{th} (V)	Current on/off ratio, I_{On}/I_{Off}	Subthreshold swing, SS ($mV\ dec^{-1}$)	Trap density N_{trap} ($1\ eV^{-1}\ cm^{-2}$)
Zr-ITO 1	8.76 ± 0.13	−2 ± 0.4	3.8 ± 0.4	6.9 (±0.5) × 10^6	660 ± 17	2.3 (±0.1) × 10^{12}
Zr-ITO 2	3.97 ± 0.08	−1 ± 0	5.9 ± 0.5	8.5 (±0.5) × 10^7	569 ± 23	2 (±0.1) × 10^{12}
Zr-ITO 3	1.92 ±0.15	0 ± 0	8.7 ± 0.3	4.4 (±0.4) × 10^7	689 ± 19	2.4 (±0.1) × 10^{12}
Hf-ITO 1	9.81 ± 0.33	−2 ± 0.5	3.3 ± 0.4	4.4 (±0.5) × 10^6	539 ± 14	1.8 (±0.1) × 10^{12}
Hf-ITO 2	5.81 ± 0.08	−1 ± 0	4.8 ± 0.1	1.1 (±0.3) × 10^8	446 ± 18	1.5 (±0.1) × 10^{12}
Hf-ITO 3	3.65 ± 0.13	0 ± 0.4	6.9 ± 0.1	1.9 (±0.2) × 10^8	534 ± 20	1.8 (±0.1) × 10^{12}
Hf/Zr-ITO	5.22 ± 0.07	−1 ± 0	5.1 ± 0.4	1.5 (±0.4) × 10^8	466 ± 18	1.6 (±0.1) × 10^{12}
Zr/Hf-ITO	5.25 ± 0.08	−1 ± 0.5	4.8 ± 0.4	2.1 (±0.8) × 10^8	484 ± 14	1.6 (±0.1) × 10^{12}

Furthermore, Figure 8b,c reveal decreasing on- and off-currents (I_{On}, I_{Off}) for both Zr-ITO and Hf-ITO with increasing amounts of Zr and Hf, respectively. However, the decline in I_{Off} is more pronounced than that of I_{On}, consequently leading to an increase in the I_{On}/I_{Off} ratio. This trend is particularly evident in the case of Hf-ITO, exhibiting an increase by two orders of magnitude when the number of Hf deposition cycles is increased, with 4.4 × 10^6 for Hf-ITO 1 and 1.9 × 10^8 for Hf-ITO 3. For Zr-ITO, an increase is also observed, although less pronounced, with an on/off ratio for Zr-ITO 1 of 6.9 × 10^6 and an increase of one order to 4.4 × 10^7 for Zr-ITO 3.

The subthreshold swing (*SS*) demonstrates a similar trend for Zr-ITO and Hf-ITO, exhibiting a decline from one to two deposition cycles and an increase from two to three cycles, reaching values comparable to one cycle or even greater (see Table 3). This phenomenon of an initial decline followed by an increase in *SS* has also been observed in our previous studies on Al-doped ITO [26] and Mg-doped ITO [25], where the trend was even more pronounced.

The TFT performance parameters for the mixed Hf/Zr- and Zr/Hf-ITO TFTs demonstrate notable comparability with each other (see Figure 8d) and also with values obtained for Zr-ITO 2 and Hf-ITO 2. The mobility values of 5.22 and 5.25 $cm^2\ V^{-1}\ s^{-1}$ for Hf/Zr- and Zr/Hf-ITO, respectively, are comparable to μ_{sat} for Hf-ITO 2 with a value of 5.81 $cm^2\ V^{-1}\ s^{-1}$, while V_{On} as well as V_{th} are similar to the values obtained for Zr- and Hf-ITO 2 with $V_{On} = -1$ V for both mixed Hf/Zr- and Zr/Hf-ITO TFTs and $V_{th} = 5.1$ and 4.8 V for Hf/Zr- and Zr/Hf-ITO, respectively. Furthermore, the on/off-ratio for Hf/Zr-ITO with 1.5×10^8 and Zr/Hf-ITO with 2.1×10^8 fall within the same range as the values obtained for Hf-ITO 2/3. Last, the *SS* values of the mixed Hf/Zr- and Zr/Hf-ITO TFTs demonstrate comparable values to those of Hf-ITO 2. At this point, it is crucial to emphasize that the deposition of the Hf/Zr-ITO thin film occurs through the exchange of every second supercycle in the Hf-ITO 2 process by a Zr-ITO 2 supercycle, and vice versa for the Zr/Hf-ITO thin film. In consideration of these factors, a comparative analysis of the performance parameters reveals that zirconium- and hafnium oxide exhibit analogous effects, suggesting their interchangeability within this particular context.

The decline of μ_{sat} and the decrease in I_{Off} with increasing amounts of dopant can be attributed to the high bond dissociation energies of zirconium oxide (766.1 ± 10.6 kJ mol^{-1}) [35, 36] and hafnium oxide (801 ± 13 kJ mol^{-1}) [35, 36]. As their bond dissociation energies are significantly higher than those of indium- and tin oxide (In—O 346 ± 30 kJ mol^{-1}, Sn—O 528 kJ mol^{-1}) [35, 36], they form stronger bonds with oxygen. Consequently, they inhibit the formation of oxygen vacancies to a significant extent, thereby hindering the generation of charge carriers. Similar observations, including a decline in mobility, a decrease in I_{Off}, and a consequent rise in I_{On}/I_{Off}, have been reported for Hf-IZO [68] and Zr-IZO TFTs [22]. For the optimized Hf-IZO TFT values of $\mu_{sat} = 3.53\ cm^2\ V^{-1}\ s^{-1}$, $V_{th} = 1.28$ V, $I_{On}/I_{Off} = 1.4 \times 10^7$, and $SS = 0.95\ V\ dec^{-1}$ were obtained [68]. In contrast, the optimized Zr-IZO TFT exhibited values of $\mu_{sat} = 3.9\ cm^2\ V^{-1}\ s^{-1}$, $V_{th} = 1.6$ V, $I_{On}/I_{Off} = 10^7$, and $SS = 0.98\ V\ dec^{-1}$ [22].

The subthreshold swing and hysteresis are both associated with the quality of the interface between the active channel (semiconductor) and the gate dielectric. A hysteresis is observed when charge trapping occurs at this particular interface, and is related to defect states [69, 70]. This correlation can be observed from the *SS* values presented in Table 3 and the hysteresis exhibited in Figure 8b–d. For Hf-ITO 1 and Zr-ITO 1, negligible hysteresis is observed, while it becomes more pronounced for Hf-ITO 2/Zr-ITO 2 and even more so for Hf-ITO 3/Zr-ITO 3. This phenomenon suggests an increase in trap states corresponding to higher amounts of Hf or Zr, respectively. Concurrently, the *SS* values undergo a slight decrease from one to two cycles and an increase from two to three. This suggests that a single cycle of Hf or Zr is insufficient to adequately passivate defect states arising from the indium tin oxide. Conversely, three cycles of Hf or Zr appear to generate an increased number of defect states. These cannot be compensated by a large number of charge carriers, as they are being suppressed concurrently. The *SS* values obtained for Hf-ITO 2 and Zr-ITO 2 with 446 and 569 mV dec^{-1}, respectively, suggest a positive trade-off between the number of charge carriers and defect states.

The trap density N_{trap} can be calculated using the following equation [71]:

$$N_{trap} = \frac{C_i}{e^2}\left(\frac{SS\ e}{kT \ln 10} - 1\right)$$

where C_i is the gate insulator capacitance per unit area, e the elementary charge, k the Boltzmann constant, and T the Temperature. With a gate insulator capacitance of 36.4 nF cm^{-2} and the *SS* values from Table 3, N_{trap} values were calculated for the doped ITO TFT devices (Table 3). The calculations reveal that both Zr-ITO 2 and Hf-ITO 2 exhibit lower trap densities compared to devices with lower or higher dopant concentrations, and is also evident for the mixed ITO devices Hf/Zr- and Zr/Hf-ITO. A comparison of N_{trap} of Zr- and Hf-ITO indicates that Hf exerts a slightly stronger influence on the density of trap states than Zr. This observation can be attributed to the higher bond dissociation energy of Hf.

The TFTs with an optimized composition are found to be Hf-ITO 2 and Zr-ITO 2, with performance parameters of $\mu_{sat} = 5.81\ cm^2\ V^{-1}\ s^{-1}$, $V_{th} = 4.8$ V, $I_{On}/I_{Off} = 1.1 \times 10^8$, and $SS = 0.45\ V\ dec^{-1}$ for Hf-ITO 2 and $\mu_{sat} = 3.97\ cm^2\ V^{-1}\ s^{-1}$, $V_{th} = 5.9$ V, $I_{On}/I_{Off} = 8.5 \times 10^7$, and $SS = 0.57\ V\ dec^{-1}$ for Zr-ITO 2. The optimized composition is also reflected in the performance parameters of the mixed Hf/Zr- and Zr/Hf-ITO TFTs, which exhibit a high degree of similarity to those of Hf-ITO 2 and Zr-ITO 2 (Table 3). Output characteristics of all investigated thin films can be found in Figure S4.

Similar trends in the TFT parameters have been observed in our earlier works on Mg-doped ITO and Al-doped ITO [25, 26]. Therefore, it can be concluded that the incorporation of an insulating component into a conductive material exerts the following effects on the TFT performance parameters: with increasing amounts of insulating component in the thin films, mobility values decline, and the current on/off-ratio exhibits a simultaneous increase. Meanwhile, the subthreshold swing demonstrates an initial decrease, followed by a subsequent increase in response to elevated levels of the insulating component. Additionally, a shift toward more positive values of the on-voltage and threshold-voltage can be observed.

Employing ALD is a valuable synthetic approach to control electronic parameters in TFT devices. Moreover, it is technologically highly relevant since it enables a reproducible introduction of atomically precise material modification in multilayer compositions. As we have shown in a series of contributions introducing oxyphilic elements, semiconducting ITO films can be modified in a highly controlled manner. A comparison on the doping of ITO reveals varying degrees of influence from each element (Table S4) [25, 26]. Doping of Aluminum even at very low

TABLE 4 | Dopants employed as carrier suppressors for the enhancement of ITO TFT devices, fabricated by various methods, along with their corresponding mobility values μ_{sat}, current on/off I_{On}/I_{Off}, and subthreshold swing *SS*.

Dopant	Mobility, μ_{sat} ($cm^2\ V^{-1}\ s^{-1}$)	Current on/off ratio, I_{On}/I_{Off}	Subthreshold swing, *SS* ($V\ dec^{-1}$)	Synthesis method	Refs.
Zirconium	3.97	8.5×10^7	0.57	ALD	This work
Hafnium/Zirconium	5.22	1.5×10^8	0.47	ALD	This work
Hafnium	5.81	1.1×10^8	0.45	ALD	This work
Hafnium	7.46	$>10^5$	0.34	Co-sputtering	[72]
Magnesium	6.45	5.3×10^7	0.64	ALD	[25]
Magnesium	52.5*	$\sim 10^7$	0.24	Co-sputtering	[73]
Aluminum	2.28	9×10^5	0.37	ALD	[26]
Titanium	13.4	$>1 \times 10^8$	0.25	Co-sputtering	[74]
Tungsten	11.53	3.3×10^7	0.66	Sputtering	[75]
Tungsten	3.86	$\sim 5.7 \times 10^6$	0.25	Spin-coating	[76]
Gallium	11.5	$>10^8$	0.33	Spin-coating	[77]
Gallium	16	$\sim 10^8$	0.13	Spray pyrolysis	[78]
Tantalum	2.37	2.5×10^8	0.45	Co-sputtering	[79]

*field-effect mobility μ_{FE}

concentrations, exerts a considerable suppression of the carrier mobility ($4.87\ cm^2\ V^{-1}\ s^{-1}$) and the current on/off ratio (4.7×10^4). Nonetheless, it exerts a positive influence on the switching ability, as evident from *SS* values as low as 365 mV dec^{-1} [26]. In contrast, doping of magnesium exerts a comparatively less pronounced effect on the TFT parameters. In the Mg-ITO system, the mobility exhibits a favorable value for the lowest amount of Mg ($10.64\ cm^2\ V^{-1}\ s^{-1}$). However, the current on/off ratio exhibits a relatively low value of 1.2×10^5 and the *SS* value is relatively high (816 mV dec^{-1}) [25]. The mobility values of both Hf- and Zr-ITO reported herein are slightly lower compared to Mg-ITO, suggesting a slightly stronger influence on the suppression of the charge carrier density. However, the current on/off ratio is higher in both Hf- and Zr-ITO, and both exhibit improved switching abilities, as evidenced by lower *SS* values (Table 3). A comparison of all doped ITO devices with the optimal composition reveals that Hf-ITO 2 exhibits the most favorable TFT parameters overall, demonstrating an adequate mobility, a high I_{On}/I_{Off}, and a satisfactory *SS* value. This comparison reveals some of the benefits and drawbacks of the four elements employed.

A comprehensive review of the literature reveals the presence of various doping elements in the ITO system. Even though the semiconducting channel can be fabricated through various processes, the main function of the different dopants is their influence to act as charge carrier suppressors. Table 4 provides a summary of dopants in ITO films as has they have been reported toward the enhancement of ITO TFT devices. A unifying characteristic feature on the introduction of these different dopants is their M—O bond dissociation energy, which typically exceeds that of indium as the main constituent [35, 36] indicating the suitability of these dopants to sufficiently suppress oxygen vacancies and as such modify the charge carrier concentration in a controlled manner.

The TFT performance parameters illustrate that a careful modulation of the ITO film composition by doping, allows to suppress charge carrier concentrations thereby reducing the off-current and achieving high on/off ratios while maintaining favorable mobility values. Conversely, achieving a high on/off ratio comes on the expense of significant compromise on the mobility.

Our work on Zr- and Hf-doped ITO exhibits comparable device parameters to those reported for other dopants reported. With their large optical band gaps and affinity toward oxygen, Zr and Hf exhibit suitable characteristics for TFT devices. Through the precise compositional control enabled by the ALD synthetic approach, elements with a high bond dissociation energy, such as Zr and Hf, can be utilized as charge carrier suppressors. Our approach supports the concept of elemental doping of a host material to tune the electronic parameters of a thin-layer composition.

To determine the charge carrier density of the fabricated thin films, Hall measurements in van der Pauw geometry were conducted. The carrier density values and their corresponding mobility values are listed in Table 5. For Zr-ITO, it is evident that the carrier density undergoes a substantial decrease from 2.8×10^{19} to $7.2 \times 10^{15}\ cm^{-3}$ as the zirconium oxide content is increased from one to three cycles. A decrease in carrier density is also apparent for increasing amounts of hafnium oxide in the Hf-ITO thin films, although less pronounced with values decreasing from 2.1×10^{19} and to $3.2 \times 10^{18}\ cm^{-3}$. Nonetheless, both mixed Hf/Zr- and Zr/Hf-ITO thin films exhibit a high carrier density,

TABLE 5 | Carrier density and corresponding mobility values for the doped ITO thin films, obtained from Hall measurements.

Sample	Mobility, μ_{sat} ($cm^2\ V^{-1}\ s^{-1}$)	Carrier density (cm^{-3})
Zr-ITO 1	8.76 ± 0.13	$2.8\ (\pm 0.09) \times 10^{19}$
Zr-ITO 2	3.97 ± 0.08	$5.5\ (\pm 0.14) \times 10^{17}$
Zr-ITO 3	1.92 ± 0.15	$7.2\ (\pm 0.74) \times 10^{15}$
Hf-ITO 1	9.81 ± 0.33	$2.1\ (\pm 0.03) \times 10^{19}$
Hf-ITO 2	5.81 ± 0.08	$9.4\ (\pm 0.27) \times 10^{18}$
Hf-ITO 3	3.65 ± 0.13	$3.2\ (\pm 0.06) \times 10^{18}$
Hf/Zr-ITO	5.22 ± 0.07	$1.9\ (\pm 0.03) \times 10^{19}$
Zr/Hf-ITO	5.25 ± 0.08	$4.5\ (\pm 0.04) \times 10^{19}$

with values of 1.9×10^{19} and 4.5×10^{19} cm^{-3} for Hf/Zr-ITO and Zr/Hf-ITO, respectively.

The obtained values for the Zr- and Hf- doped ITO thin films fall within the range of reported values for IGZO films of varying quality, with 10^{16}–10^{20} cm^{-3} [80] and can also be compared to those determined for Mg-doped ITO thin films from our previous studies, with values ranging between 1.1×10^{19}–5.9×10^{19} cm^{-3} [25].

Finally, a systematic view on the dependency on the charge carrier mobilities μs_{at} as well as the experimental charge carrier densities of the different zirconium and hafnium doped ITO thin films with increasing dopant concentration is intriguing and even possible for the magnesium and aluminum doped ITO TFTs (see Table 5; Table S4) [25, 26]. The overall electron mobility μ decreases monotonically for all twelve TFTs with increasing dopant concentration for all devices. This behavior can be correlated with a quantitative oxophilicity scale [81], in which oxophilicity values Φ are decreasing from Hf (1.0) to Zr (0.8), Al (0.8), and Mg (0.6), being the largest for Hf of all elements [81]. On the other hand, Φ values for In (0.4) and Sn (0.4) are significantly lower for both elements [81]. The effect of diminishing electron mobilities can be best understood by a suppression of the free charge carrier concentrations, which is primarily controlled by the steadily increasing incorporation of the stronger oxygen binding cationic dopants in the different film compositions. A similar monotonous decrease upon increasing dopant ratio is also reflected in the I_{On}/I_{Off} parameters, whereas an increase of V_{th} is observed for all twelve TFT devices upon increasing cationic dopant concentration.

Metal oxide semiconductors have been demonstrated to exhibit distinctive carrier transport mechanisms; a phenomenon attributed to their unique electronic structure. The conduction band minimum (CBM) is primarily composed of unoccupied metal cation *s* orbitals, while the VBM is constituted by fully occupied oxygen 2*p* orbitals [82]. It has been established that, due to the spherical nature of the *s* orbitals and their consequent substantial spatial expansion, structural disorder does not impact their overlap with neighboring *s* orbitals. Consequently, electron transport remains unaffected even in amorphous materials [82, 83]. However, the presence of disorder can result in the emergence of localized states within the band gap, such as tail states. For instance, in an In_2O_3 lattice, the replacement of an In atom with a Hf atom results in a higher degree of disorder in the lattice. Hf exhibits a higher bond-dissociation energy, which leads to its stronger attraction of oxygen ions, resulting in a shortening of the M—O bond [84]. These localized states, as well as the position of the Fermi-level (E_F), have the capacity to exert a significant influence on the carrier transport mechanism. In the event where the density of traps exceeds the density of free charge carriers or at low gate voltages (V_{GS}), E_F is incapable of crossing the conduction band edge, resulting in its localization within the subgap states. In this instance, the charge transport is governed by a succession of trapping and thermal release events, referred to as trap-limited conduction (TLC) [84, 85]. However, if the density of free carriers exceeds the density of traps, and at high V_{GS}, E_F crosses the conduction band edge, thereby filling all trap states. In this scenario, the charge transport is exclusively

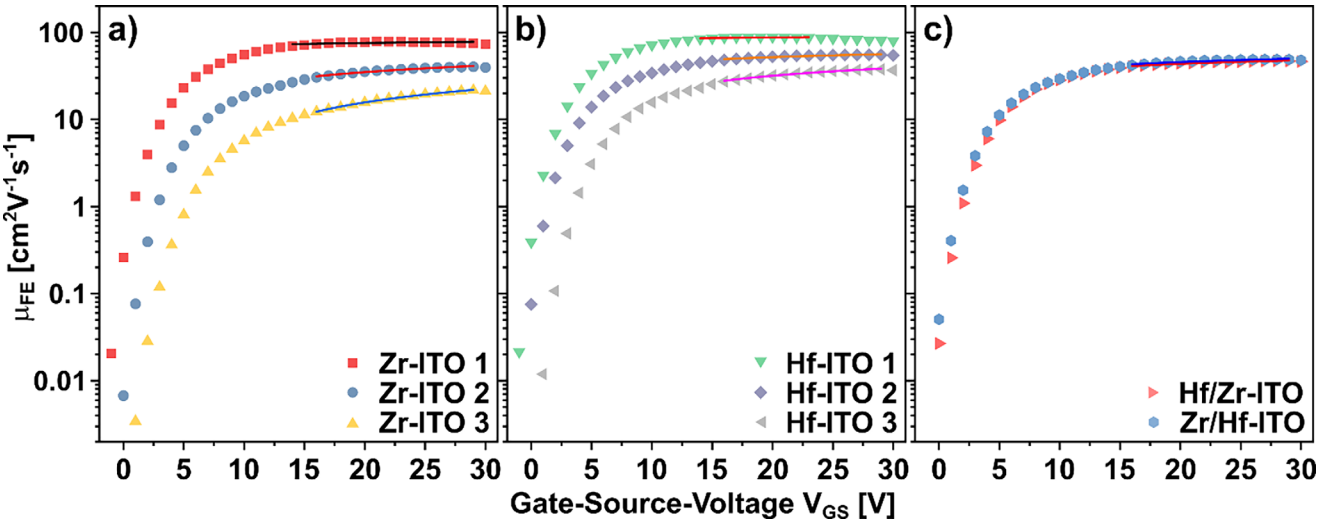

FIGURE 9 | Dependency of the field-effect mobility (μ_{FE}) on the gate-source-voltage (V_{GS}) for (a) Zr-ITO, (b) Hf-ITO, and (c) mixed Hf/Zr- and Zr/Hf-ITO, including the corresponding power–law fits to obtain values for γ.

TABLE 6 | Values for γ and the mobility (μ_{FE}) with their corresponding standard deviation for the doped ITO heterostructures, including their dominant conduction mechanism.

Sample	γ	Mobility μ ($cm^2\ V^{-1}\ s^{-1}$)	Conduction mechanism
Zr-ITO 1	0.07 ± 0.02	8.76 ± 0.13	PC
Zr-ITO 2	0.33 ± 0.01	3.97 ± 0.08	PC/TLC
Zr-ITO 3	0.57 ± 0.01	1.92 ± 0.15	PC/TLC
Hf-ITO 1	0.04 ± 0.01	9.81 ± 0.33	PC
Hf-ITO 2	0.17 ± 0.01	5.81 ± 0.08	PC/TLC
Hf-ITO 3	0.36 ± 0.01	3.65 ± 0.13	PC/TLC
Hf/Zr-ITO	0.18 ± 0.01	5.22 ± 0.07	PC/TLC
Zr/Hf-ITO	0.19 ± 0.01	5.25 ± 0.08	PC/TLC

determined by the movement of electrons over the distribution of potential barriers within the conduction band, referred to as percolation conduction [84, 85].

The predominant charge carrier transport mechanism of the doped ITO TFTs is determined through applying a power law fit to the field-effect mobility as a function of the gate voltage (Figure 9).

$$\mu_{FE} = K\left(V_{GS} - V_{th,P}\right)^{\gamma} \quad (1)$$

with the prefactor K, V_{GS}, V_{th}, V_P denoting the gate-, threshold-, and percolation voltage, respectively, and the exponent γ, correlated to the prevailing conduction mechanism. The value of γ provides insight into the transport mechanism. When γ reaches values of 0.7 or higher, the charge transport is governed by TLC. While values of 0.1 or lower indicate a PC dominated transport mechanism [83]. The boundaries of these mechanisms are diffuse and appear blurred in the range between 0.1 and 0.7. In Table 6, the values obtained for γ and μ_{FE} are summarized, and the prevalent transport mechanism is denoted.

The TFTs Zr-ITO 1 and Hf-ITO 1 both demonstrate a distinctly PC-dominated charge transport mechanism, with γ values of 0.07 and 0.04, respectively. As the amount of Zr and Hf increases, the resulting γ values exhibit a corresponding shift toward the boundaries of the PC regime and beyond. However, no distinct TLC-dominated transport mechanism is discernable. This shift is evidenced by the values of 0.33 for Zr-ITO 2 and 0.57 for Zr-ITO 3, and 0.17 for Hf-ITO 2 and 0.36 for Hf-ITO 3, respectively. The mixed Hf/Zr- and Zr/Hf-ITO TFTs, Hf/Zr-ITO and Zr/Hf-ITO, exhibit γ values of 0.18 and 0.19, respectively, which are comparable to the γ value of Hf-ITO 2. This suggests that Hf exerts a more pronounced influence on the transport mechanism compared to Zr.

It is crucial to note the discrepancy in the GPC for Zr and Hf during the deposition process. The GPC for zirconium oxide from $Zr(NMe_2)_4$ and water was calculated to be 0.87 Å/C, whereas for hafnium oxide from $Hf(NEt_2)_4$ and water, the GPC was calculated to be 0.63 Å/C. As a consequence of this discrepancy, the incorporation of Zr or Hf into the thin film is found to vary, even when the same number of supercycles are employed. The XPS analysis provides further insight into this matter. In the case of two supercycles, Zr-ITO 2 exhibits a Zr content of 3.7 at%, while Hf-ITO 2 displays a Hf content of 2.9 at%. This observation demonstrates that a higher GPC results in increased deposition of the respective material. Therefore, the similarity of the γ values for Hf-ITO 3 and Zr-ITO 2 can be explained by their comparable Hf or Zr contents, with 3.9 and 3.7 at%, respectively. This phenomenon can also provide a rationale for the more pronounced increase of γ observed in the Zr-ITO TFTs. Moreover, it has been observed that the fabrication process by ALD has a profound influence over the control of the charge transport mechanism.

3 | Conclusion

Heterostack architectures consisting of a combination of conducting and insulating metal oxides have been fabricated via ALD. The doping of ITO thin films with either zirconium or hafnium or mixtures of both yielded semiconducting thin films which were successfully implemented as an active channel layer in TFT devices. Thin film deposition was performed at 200°C, utilizing trimethylindium, tetrakisdimethylamidotin(IV), tetrakisdimethylamidozirconium(IV), and tetrakisdiethylamidohafnium(IV) as metal precursors, with water serving as oxidizing agent. The doped ITO thin films were found to be smooth, with R_{RMS} values below 0.33 nm, exhibiting a high optical transparency of ≥89% and a broadening of the optical band gap corresponding to increasing amounts of Zr and Hf in the respective thin films. GI-XTS analysis revealed amorphous, disordered structures with a correlation length of ~13 Å for Zr-ITO and ~10 Å for Hf-ITO, with the low r region correlating with crystalline ITO reference structures. Through the implementation of the Zr- and Hf-doped ITO thin films into TFT devices, their suitability as an active channel layer and the influence of Zr and Hf on the device performance were investigated. The optimized composition for Hf- and Zr-doped ITO thin films was found to be Hf-ITO 2 and Zr-ITO 2, with their respective performance parameters of μ_{sat} = 5.81 $cm^2\ V^{-1}\ s^{-1}$, V_{th} = 4.8 V, $I_{On}/I_{Off} = 1.1 \times 10^8$, and SS = 0.45 V dec^{-1} for Hf-ITO 2 and μ_{sat} = 3.97 $cm^2\ V^{-1}\ s^{-1}$, V_{th} = 5.9 V, $I_{On}/I_{Off} = 8.5 \times 10^7$, and SS = 0.57 V dec^{-1} for Zr-ITO 2. The fabrication of TFTs incorporating both elements was achieved by alternating the ALD supercycles of Hf-ITO 2 and Zr-ITO 2, yielding Hf/Zr-ITO and Zr/Hf-ITO thin films. The respective TFTs demonstrated performance parameters comparable to those of Hf-ITO 2 and Zr-ITO 2, thus indicating that the equal incorporation of both Zr and Hf exerts a purely substitutional effect. The electronic parameters of the thin films demonstrated a decrease in charge carrier density with increasing amounts of Zr and Hf, thereby indicating their efficacy in suppressing the formation of oxygen vacancies. Consequently, zirconium and hafnium oxide are promising alternatives to Ga_2O_3 as a charge carrier-suppressing oxide. The findings of the present study demonstrate the applicability of a conducting/insulating material combination to obtain a semiconducting material. Furthermore, the results demonstrate a significant correlation between the composition of the active channel layer and the TFT performance parameters. Consequently, ALD was selected as the fabrication method of choice, given its ability to deposit each layer individually, enabling precise control over the cation distribution and the film thickness.

4 | Experimental Section

4.1 | Methods

All depositions were conducted at 200°C employing a Savannah S100 (Cambridge Ultratech) ALD system at a base pressure of 4 torr. Prior to the deposition process, the substrates were maintained within the reaction chamber at 200°C for a period of 20 min under a constant argon flow of 20 sccm.

As metal precursors trimethylindium (TMI, 99.999%, AkzoNobel) was utilized for indium oxide, tetrakisdimethylamidotin(IV) (TDMASn) [86] for tin oxide, tetrakisdimethylamidozirconium (IV) (TDMAZr) [87] for zirconium oxide, and tetrakisdiethylamidohafnium(IV) (TDEAHf) [88] for hafnium oxide. Water (HPLC grade, Sigma-Aldrich) was utilized as the oxidizing agent. TMI and water were kept at room temperature, while TDMASn, TDMAZr, and TDEAHf were heated to 60°C, 75°C, and 130°C, respectively. Argon (99.9999%, AlphaGaz) was utilized as carrier gas, with a constant flow rate of 20 sccm maintained throughout the deposition process.

The deposition sequences for each metal oxide are given hereafter: Indium oxide: TMI pulse 0.1 s, exposition time 1.5 s, Ar purge 20 s, water pulse 0.1 s, exposition time 1.5 s, Ar purge 20 s. Tin oxide: TDMASn pulse 0.5 s, exposition time 1.5 s, Ar purge 30 s, water pulse 0.015 s, exposition time 1.5 s, Ar purge 30 s. Zirconium oxide: TDMAZr pulse 0.25 s, exposition time 1.5 s, Ar purge 20 s, water 0.015 s, exposition time 1.5 s, Ar purge 30 s. Hafnium oxide: TDEAHf pulse 0.2 s, exposition time 1.5 s, Ar purge 30 s, water 0.015 s, exposition time 1.5 s, Ar purge 30 s.

For both Hf-ITO and Zr-ITO, the TMI and TDMASn cycles were maintained at a constant number of 26 and 15, respectively, while the number of TDEAHf and TDMAZr cycles was subjected to variation between one and three. The deposition sequence of 26 cycles TMI, 15 cycles TDMASn, and one to three cycles TDMAZr or TDEAHf was referred to as a super cycle. This super cycle was repeated eight times in order to achieve an optimal film thickness. In the case of Zr/Hf-ITO (Hf/Zr-ITO), one super cycle consisted of 26 cycles TMI, 15 cycles TDMASn, 2 cycles TDMAZr (TDEAHf), 26 cycles TMI, 15 cycles TDMASn, and 2 cycles TDEAHf (TDMAZr). Given that one super cycle for the mixed Hf/Zr- and Zr/Hf-ITO phases was twice the amount compared to Hf-ITO or Zr-ITO, the super cycle was repeated only four times to achieve a comparable overall film thickness.

4.2 | Material Characterization

UV–vis characterization was performed within a wavelength range of 190–900 nm, using an Evolution 600 spectrometer (Thermo Scientific). Coated and annealed (40 min @ 350°C) quartz substrates were used as samples. Ellipsometry was used to obtain the film thicknesses, employing a spectroscopic ellipsometer M2000 (J.A. Woollam) in a spectral range of 370–1690 nm and an angular range of 45°–85°. Coated and annealed (40 min @ 350°C) Si/SiO_2 substrates were used as samples.

HRTEM was performed with a FEI Tecnai G2 F20 with an operating voltage of 200 keV [89]. Samples for FIB were prepared using a gallium-focused ion beam (FEI Helios NanoLab 460F1 FIB-SEM) and a subsequent coating with a platinum layer [90]. Coated and annealed (40 min @ 350°C) TFT substrates, which were electrically characterized beforehand, were used as samples.

X-ray photoelectron spectroscopy (XPS) measurements were performed using a K-Alpha+ XPS spectrometer (ThermoFisher Scientific, East Grinstead, UK) using the Thermo Avantage software for data acquisition and processing. All samples were analyzed using a microfocused, monochromated Al Kα X-ray source (400 µm spot size). The K-Alpha+ charge compensation system was employed during analysis, using electrons of 8 eV energy, and low-energy argon ions to prevent any localized charge build-up. The spectra were fitted with one or more Voigt profiles (BE uncertainty: ±0.2 eV) and Scofield sensitivity factors were applied for quantification [91]. All spectra were referenced to the C 1*s* peak (C—C, C—H) at 285 eV binding energy controlled by means of the well-known photoelectron peaks of metallic Cu, Ag, and Au, respectively. Coated and annealed (40 min @ 350°C) Si/SiO_2 substrates were used as samples.

Grazing incidence X-ray total scattering (GI-XTS) measurements were conducted at beamline P21.1 at the storage ring PETRA III, DESY, Germany. The X-ray beam of 101.4 keV was focused by means of compound refractive lenses to a size of ≈2 × 150 µm^2 (vertical by horizontal) [92]. A Pilatus3 X CdTe 2M hybrid pixel detector was mounted at a sample distance of ≈300 mm. Data were collected through a single exposure at an incidence angle of ∼0.015° with an optimized signal-to-background ratio. For the azimuthal integration of the 2D diffraction patterns pyFAI [93] was used, while the conversion into the PDF was carried out using PDFgetX3 [94] implemented into the xPDFsuite package [95]. Coated and annealed (40 min @ 350°C) quartz substrates were used as samples. Samples studied were deposited in eight super cycles, as described above, with two, four, and six cycles of zirconium oxide (Zr-ITO 2, 4, 6) or hafnium oxide (Hf-ITO 2, 4, 6). Film thicknesses ranged from 8.3–10.9 nm for Zr-ITO and 9.7–11.4 nm for Hf-ITO, respectively.

Atomic force microscopy (AFM) measurements were conducted on a Bruker Dimension ICON (Santa Barbara, CA) in tapping mode (repulsive regime) using a PPP-FM-Au cantilever (Nanosensors, Neuchatel, Switzerland) with a nominal spring constant of 3 N/m and resonance frequency of 75 kHz. The free oscillation amplitude was approx. 135 nm at a setpoint ratio of 0.6 (A_{sp}/A_0). These amplitudes were calibrated by pushing the vibrating cantilever against a stiff sapphire sample and recording the linear decrease in amplitude with respect to the z-piezo motion. Images were recorded at a line rate of 1 Hz and the digital resolution corresponds to 512 × 512 pixels. For each sample, the root mean square roughness R_{RMS} was determined as the average of three independent 1 × 1 µm^2 areas. Coated and annealed (40 min @ 350°C) Si/SiO_2 substrates were used as samples.

4.3 | Electrical Characterization

As TFT substrates, commercial substrates (Fraunhofer IMPS, Dresden) in a BGBC device geometry with prefabricated source-drain electrodes were used [96]. These consisted of highly n-doped silicon with a 90 nm layer of SiO_2. The source-drain

electrodes were composed of gold (40 nm) with an ITO adhesion layer (10 nm) below, exhibiting an interdigital structure with a channel length of $L = 20$ µm and channel width of $W = 10$ mm ($W/L = 500$).

All substrates (TFT, quartz, Si/SiO_2) were cleaned via ultrasonication for a duration of 10 min, using acetone, water, and isopropanol (HPLC grades, Carl Roth GmbH & Co. KG) subsequently and dried at 55°C for a minimum of 24 h. Prior to the deposition, all substrates underwent UV treatment using a UV ozone cleaner (UV Ozone Cleaner UVC-1014, NanoBioAnalytics) for a duration of 10 min, with a wavelength of 254 nm and an optical power of 4 W [97]. A B1500A Semiconductor Device Analyzer (Agilent Technologies) was employed for TFT measurements, which were conducted inside a glovebox ($O_2 < 0.5$ ppm, $H_2O < 0.5$ ppm) in an argon atmosphere, under the exclusion of white light. Prior to IV-measurements, TFT samples were subjected to an annealing process on a ceramic hotplate for a period of 40 min at 350°C in an ambient atmosphere. The charge carrier mobility (μs_{at}) and the threshold voltage (V_{th}) were extracted from a linear fit of the square root of the source-drain current (I_{DS}), as a function of the gate-source voltage (V_{GS}). A total of eight (8) transistors were measured for each composition, fabricated in two independent ALD processes.

Hall measurements were conducted as four-point measurements utilizing the Van der Pauw geometry at ambient temperature. A magnetic field of 1.3 T was established, with a current range spanning from 1×10^{-4} to 5×10^{-2} mA. A LakeShore EM4-HVA magnet with 52 mm pole caps with a LakeShore Model 643 Electromagnet power supply was used. The magnet and power supply were water-cooled. The magnetic field was controlled by a LakeShore 475 DSP Gaussmeter, and the currents for the measurements were provided by a Keithley 2635A System SourceMeter. Additionally, a Keithley 2700 Multimeter with an installed 7709 Switching Card was used. Coated and annealed (40 min @ 350°C) quartz substrates, with sputtered Pt/Pd contacts (80 nm) on all four corners, were used as samples.

Acknowledgements

TEM sample preparation and measurements were done at the Ernst-Ruska Center (ERC) Jülich under contract ERC-TUDa. We thank Jörg Engstler (TUDa) for partial experimental assistance and TEM measurement. The authors are grateful to Alexander Creutz for the assistance with Hall measurements and to Andreas Klein, both at the Department of Materials Science at TUDa for giving the opportunity to measure our samples. Parts of this research were carried out at beamline P21.1 at PETRA III at DESY. We acknowledge DESY (Hamburg, Germany), a member of the Helmholtz Association HGF, for the provision of experimental facilities. We acknowledge funding for the beamline's focusing optics through BMBF grant 05K22RF1. Work of MIB and JJS is funded by the Deutsche Forschungsgemeinschaft (DFG, German Research Foundation) under project SCHN 375 46-1.

Open access funding enabled and organized by Projekt DEAL.

Conflicts of Interest

The authors declare no conflict of interest.

Data Availability Statement

The data that support the findings of this study are available from the corresponding author upon reasonable request.

References

1. J. Y. Noh, D. M. Han, W. C. Jeong, J. W. Kim, and S. Y. Cha, "Development of 55″ 4K UHD OLED TV Employing the Internal Gate IC with High Reliability and Short Channel IGZO TFTs," *Journal of the Society for Information Display* 26 (2018): 36–41, https://doi.org/10.1002/jsid.628.

2. C.-W. Han, J.-S. Park, H.-S. Choi, et al., "Advanced Technologies for UHD Curved OLED TV," *Journal of the Society for Information Display* 22 (2014): 552–563, https://doi.org/10.1002/jsid.287.

3. S. Ji, J. Jang, J. C. Hwang, Y. Lee, J.-H. Lee, and J.-U. Park, "Amorphous Oxide Semiconductor Transistors With Air Dielectrics for Transparent and Wearable Pressure Sensor Arrays," *Advanced Materials Technologies* 5 (2020): 1900928, https://doi.org/10.1002/admt.201900928.

4. B. Wang, G. M. Biesold, M. Zhang, and Z. Lin, "Amorphous Inorganic Semiconductors for the Development of Solar Cell, Photoelectrocatalytic and Photocatalytic Applications," *Chemical Society Reviews* 50 (2021): 6914–6949, https://doi.org/10.1039/D0CS01134G.

5. K. Nomura, H. Ohta, A. Takagi, T. Kamiya, M. Hirano, and H. Hosono, "Room-Temperature Fabrication of Transparent Flexible Thin-Film Transistors Using Amorphous Oxide Semiconductors," *Nature* 432 (2004): 488–492, https://doi.org/10.1038/nature03090.

6. Y.-C. Chang, S.-T. Wang, Y.-T. Lee, et al., "Breaking the Trade-Off Between Mobility and On–Off Ratio in Oxide Transistors," *Advanced Materials* 37 (2025): 2413212, https://doi.org/10.1002/adma.202413212.

7. J. Sheng, H.-J. Jeong, K.-L. Han, T. Hong, and J.-S. Park, "Review of Recent Advances in Flexible Oxide Semiconductor Thin-Film Transistors," *Journal of Information Display* 18 (2017): 159–172, https://doi.org/10.1080/15980316.2017.1385544.

8. H. G. Kim, H. J. Lee, K. M. Lee, and T. G. Kim, "Improved Mobility and Bias Stability of Hf-Doped IGZO/IZO/Hf-Doped IGZO Thin-Film Transistor," *Journal of Alloys and Compounds* 981 (2024): 173587, https://doi.org/10.1016/j.jallcom.2024.173587.

9. Y.-L. Wang, F. Ren, W. Lim, et al., "Room Temperature Deposited Indium Zinc Oxide Thin Film Transistors," *Applied Physics Letters* 90 (2007): 232103, https://doi.org/10.1063/1.2746084.

10. S. Sanctis, J. Krausmann, C. Guhl, and J. J. Schneider, "Stacked Indium Oxide/Zinc Oxide Heterostructures as Semiconductors in Thin Film Transistor Devices: A Case Study Using Atomic Layer Deposition," *Journal of Materials Chemistry C* 6 (2018): 464–472.

11. I.-H. Baek, J. J. Pyeon, S. H. Han, et al., "High-Performance Thin-Film Transistors of Quaternary Indium–Zinc–Tin Oxide Films Grown by Atomic Layer Deposition," *ACS Applied Materials & Interfaces* 11 (2019): 14892–14901, https://doi.org/10.1021/acsami.9b03331.

12. G.-B. Kim, N. On, T. Kim, et al., "High Mobility IZTO Thin-Film Transistors Based on Spinel Phase Formation at Low Temperature Through a Catalytic Chemical Reaction," *Small Methods* 7 (2023): 2201522, https://doi.org/10.1002/smtd.202201522.

13. S. Cho, J.-H. Yang, J. G. Oh, et al., "The Role of Oxygen in Dramatically Enhancing the Electrical Properties of Solution-Processed Zn–Sn–O Thin-Film Transistors," *Journal of Materials Chemistry C* 5 (2017): 6521–6526, https://doi.org/10.1039/C7TC01190C.

14. W.-C. Jhang, P.-H. Chen, C.-C. Hsu, and U. Nanda, "Performance Improvement of a Sol–Gel ZTO-Based TFT due to an Interfacial SnO_x Dopant Layer," *Journal of Materials Chemistry C* 11 (2023): 5750–5761, https://doi.org/10.1039/D3TC00422H.

15. D.-H. Cho, S. Yang, C. Byun, et al., "Transparent Al–Zn–Sn–O Thin Film Transistors Prepared at Low Temperature," *Applied Physics Letters* 93 (2008): 142111, https://doi.org/10.1063/1.2998612.

16. G. H. Kim, B. Du Ahn, H. S. Shin, W. H. Jeong, H. J. Kim, and H. J. Kim, "Effect of Indium Composition Ratio on Solution-Processed Nanocrystalline InGaZnO Thin Film Transistors," *Applied Physics Letters* 94 (2009): 233501, https://doi.org/10.1063/1.3151827.

17. M. H. Cho, M. J. Kim, H. Seul, et al., "Impact of Cation Compositions on the Performance of Thin-Film Transistors With Amorphous Indium Gallium Zinc Oxide Grown Through Atomic Layer Deposition," *Journal of Information Display* 20 (2019): 73–80, https://doi.org/10.1080/15980316.2018.1540365.

18. J. Liu, S. Liu, Y. Yu, et al., "High Mobility and Photo-Bias Stable Metal Oxide Thin-Film Transistors Engineered by Gradient Doping," *Advanced Electronic Materials* 8 (2022): 2100984, https://doi.org/10.1002/aelm.202100984.

19. Y.-S. Kim, W.-B. Lee, H.-J. Oh, T. Hong, and J.-S. Park, "Remarkable Stability Improvement with a High-Performance PEALD-IZO/IGZO Top-Gate Thin-Film Transistor via Modulating Dual-Channel Effects," *Advanced Materials Interfaces* 9 (2022): 2200501, https://doi.org/10.1002/admi.202200501.

20. C.-X. Huang, J. Li, Y.-Z. Fu, J.-H. Zhang, X.-Y. Jiang, and Z.-L. Zhang, "Suppression in the Negative Bias Illumination Instability of ZnSnO Thin-Film Transistors Using Hafnium Doping by Dual-Target Magnetron Cosputtering System," *IEEE Transactions on Electron Devices* 63 (2016): 3552–3557, https://doi.org/10.1109/ted.2016.2589240.

21. H. Woo and S. Jeon, "Microsecond Pulse I–V Approach to Understanding Defects in High Mobility Bi-Layer Oxide Semiconductor Transistor," *Scientific Reports* 7 (2017): 8235, https://doi.org/10.1038/s41598-017-06613-1.

22. J.-S. Park, K. Kim, Y.-G. Park, Y.-G. Mo, H. D. Kim, and J. K. Jeong, "Novel ZrInZnO Thin-Film Transistor With Excellent Stability," *Advanced Materials* 21 (2009): 329–333, https://doi.org/10.1002/adma.200802246.

23. A. Abliz, L. Xu, D. Wan, et al., "Effects of Yttrium Doping on the Electrical Performances and Stability of ZnO Thin-Film Transistors," *Applied Surface Science* 475 (2019): 565–570, https://doi.org/10.1016/j.apsusc.2018.12.236.

24. G. H. Kim, W. H. Jeong, B. Du Ahn, et al., "Investigation of the Effects of Mg Incorporation into InZnO for High-Performance and High-Stability Solution-Processed Thin Film Transistors," *Applied Physics Letters* 96 (2010): 163506, https://doi.org/10.1063/1.3413939.

25. M. I. Büschges, V. Trouillet, A.-C. Dippel, and J. J. Schneider, "Amorphous Doped Indium Tin Oxide Thin-Films by Atomic Layer Deposition. Insights into Their Structural, Electronic and Device Reliability," *Advanced Materials Interfaces* 12 (2025): 2400758, https://doi.org/10.1002/admi.202400758.

26. M. I. Büschges, V. Trouillet, and J. J. Schneider, "Electronic Influence of Ultrathin Aluminum Oxide on the Transistor Device Performance of Binary Indium/Tin Oxide Films," *Journal of Materials Chemistry C* 10 (2022): 5447–5457, https://doi.org/10.1039/D2TC00285J.

27. H.-M. Kim, D.-G. Kim, Y.-S. Kim, M. Kim, and J.-S. Park, "Atomic Layer Deposition for Nanoscale Oxide Semiconductor Thin Film Transistors: Review and Outlook," *International Journal of Extreme Manufacturing* 5 (2023): 012006, https://doi.org/10.1088/2631-7990/acb46d.

28. R. W. Johnson, A. Hultqvist, and S. F. Bent, "A Brief Review of Atomic Layer Deposition: From Fundamentals to Applications," *Materials Today* 17 (2014): 236–246, https://doi.org/10.1016/j.mattod.2014.04.026.

29. S. M. George, "Atomic Layer Deposition: An Overview," *Chemical Reviews* 110 (2010): 111–131, https://doi.org/10.1021/cr900056b.

30. J. Wu, H. Zheng, M. Guo, et al., "Enhancing Temperature Stability of ALD-Deposited IGZO Thin-Film Transistor by Optimizing Composition Ratio," *Journal of Alloys and Compounds* 1022 (2025): 179753, https://doi.org/10.1016/j.jallcom.2025.179753.

31. S. Feliu and M. L. Pérez-Revenga, "Effect of the Presence of Alloying Elements in Interstitial-Free and Low-Carbon Steels on Their Surface Composition After Annealing in Reducing Atmospheres (Dew Point = −30 °C)," *Metallurgical and Materials Transactions A* 35 (2004): 2039–2050, https://doi.org/10.1007/s11661-004-0152-2.

32. D. Barreca, G. A. Battiston, R. Gerbasi, E. Tondello, and P. Zanella, "Zirconium Dioxide Thin Films Characterized by XPS," *Surface Science Spectra* 7 (2000): 303–309, https://doi.org/10.1116/1.1375573.

33. J. K. Mathiesen, J. Zhu, W. Wan, S. Shaikhutdinov, and B. R. Cuenya, "Metal–Support Interaction in In_2O_3-Based Catalysts of CO_2 Hydrogenation Studied Using "Inverse" In_2O_3 (111)/Ru(0001) Model Systems," *The Journal of Physical Chemistry C* 129 (2025): 8582–8590, https://doi.org/10.1021/acs.jpcc.5c00272.

34. K. Tetzner, I. Isakov, A. Regoutz, D. J. Payne, and T. D. Anthopoulos, "The Impact of Post-Deposition Annealing on the Performance of Solution-Processed Single Layer In_2O_3 and Isotype In_2O_3/ZnO Heterojunction Transistors," *Journal of Materials Chemistry C* 5 (2017): 59–64.

35. Y.-R. Luo, *Comprehensive Handbook of Chemical Bond Energies* (CRC Press Taylor & Francis, 2007).

36. Y.-R. Luo and J. A. Kerr, *Bond Dissociation Energies*, 89th ed. (CRC Taylor & Francis, 2012), 65–98.

37. F. A. Akgul, C. Gumus, A. O. Er, et al., "Structural and Electronic Properties of SnO_2," *Journal of Alloys and Compounds* 579 (2013): 50–56, https://doi.org/10.1016/j.jallcom.2013.05.057.

38. S. X. Lao, R. M. Martin, and J. P. Chang, "Plasma Enhanced Atomic Layer Deposition of HfO_2 and ZrO_2 High-k Thin Films," *Journal of Vacuum Science & Technology A: Vacuum, Surfaces, and Films* 23 (2005): 488–496, https://doi.org/10.1116/1.1894666.

39. G. Greczynski and L. Hultman, "Impact of Sample Storage Type on Adventitious Carbon and Native Oxide Growth: X-Ray Photoelectron Spectroscopy Study," *Vacuum* 205 (2022): 111463, https://doi.org/10.1016/j.vacuum.2022.111463.

40. P. Simon, V. G. Baldovino-Medrano, and R. Wojcieszak, "X-Ray Photoelectron Spectroscopy (XPS): Principles and Application for the Analysis of Photoactive Materials," in *Springer Handbook of Inorganic Photochemistry*, eds. D. Bahnemann and A.O.T. Patrocinio (Springer International Publishing, 2022), 249–271.

41. S. Feliu Jr, M. C. Merino, R. Arrabal, A. E. Coy, and E. Matykina, "XPS Study of the Effect of Aluminium on the Atmospheric Corrosion of the AZ31 Magnesium Alloy," *Surface and Interface Analysis* 41 (2009): 143–150, https://doi.org/10.1002/sia.3004.

42. D.-Y. Cho, H.-S. Jung, and C. S. Hwang, "Structural Properties and Electronic Structure of HfO_2-ZrO_2 Composite Films," *Physical Review B* 82 (2010): 094104, https://doi.org/10.1103/PhysRevB.82.094104.

43. T. Nabatame, E. Maeda, M. Inoue, et al., "Influence of HfO2 and SiO_2 Interfacial Layers on the Characteristics of n-GaN/$HfSiO_X$ Capacitors Using Plasma-Enhanced Atomic Layer Deposition," *Journal of Vacuum Science & Technology A: Vacuum, Surfaces, and Films* 39 (2021): 062405, https://doi.org/10.1116/6.0001334.

44. D. C. Hays, B. P. Gila, E. S. Lambers, S. J. Pearton, and F. Ren, "Valence and Conduction Band Offsets in Sputtered HfO_2/$InGaZnO_4$ Heterostructures," *Vacuum* 116 (2015): 60–64, https://doi.org/10.1016/j.vacuum.2015.02.017.

45. W. Wang, H. Dong, M. Wang, et al., "Thermoelectric Properties and Microscopic Characterization of Hf Doped Indium Oxide Thick Film Thermocouples Screen Printed on Alumina Substrates," *Journal of the European Ceramic Society* 44 (2024): 3937–3944, https://doi.org/10.1016/j.jeurceramsoc.2023.12.103.

46. Z. M. Detweiler, S. M. Wulfsberg, M. G. Frith, A. B. Bocarsly, and S. L. Bernasek, "The Oxidation and Surface Speciation of Indium and Indium Oxides Exposed to Atmospheric Oxidants," *Surface Science* 648 (2016): 188–195, https://doi.org/10.1016/j.susc.2015.10.026.

47. S. D. Ponja, B. A. D. Williamson, S. Sathasivam, D. O. Scanlon, I. P. Parkin, and C. J. Carmalt, "Enhanced Electrical Properties of Antimony Doped Tin Oxide Thin Films Deposited via Aerosol Assisted Chemical

Vapour Deposition," *Journal of Materials Chemistry C* 6 (2018): 7257–7266, https://doi.org/10.1039/C8TC01929K.

48. F. Borgatti, J. A. Berger, D. Céolin, et al., "Revisiting the Origin of Satellites in Core-Level Photoemission of Transparent Conducting Oxides: The Case of n-Doped SnO_2," *Physical Review B* 97 (2018): 155102, https://doi.org/10.1103/PhysRevB.97.155102.

49. V. Kumar, N. Singh, R. M. Mehra, A. Kapoor, L. P. Purohit, and H. C. Swart, "Role of Film Thickness on the Properties of ZnO Thin Films Grown by Sol-Gel Method," *Thin Solid Films* 539 (2013): 161–165, https://doi.org/10.1016/j.tsf.2013.05.088.

50. J.-P. Xu, R.-J. Zhang, Y. Zhang, et al., "The Thickness-dependent Band Gap and Defect Features of Ultrathin ZrO_2 Films Studied by Spectroscopic Ellipsometry," *Physical Chemistry Chemical Physics* 18 (2016): 3316–3321, https://doi.org/10.1039/c5cp05592j.

51. R. Yusoh, M. Horprathum, P. Eiamchai, P. Chindaudom, and K. Aiempanakit, "Determination of Optical and Physical Properties of ZrO_2 Films by Spectroscopic Ellipsometry," *Procedia Engineering* 32 (2012): 745–751, https://doi.org/10.1016/j.proeng.2012.02.007.

52. F. L. Martínez, M. Toledano-Luque, J. J. Gandía, et al., "Optical Properties and Structure of HfO_2 Thin Films Grown by High Pressure Reactive Sputtering," *Journal of Physics D: Applied Physics* 40 (2007): 5256–5265, https://doi.org/10.1088/0022-3727/40/17/037.

53. R. K. Nahar, V. Singh, and A. Sharma, "Study of Electrical and Microstructure Properties of High Dielectric Hafnium Oxide Thin Film for MOS Devices," *Journal of Materials Science: Materials in Electronics* 18 (2007): 615–619, https://doi.org/10.1007/s10854-006-9111-6.

54. X. Bi, J. Yao, and S. Zhang, "Magnesium-Doped Indium Oxide Thin Film Transistors for Ultraviolet Detection," in 2014 IEEE International Conference on Electron Devices and Solid-State Circuits (EDSSC 2014): Chengdu, China, 18 –20 June 2014, Piscataway, NJ (IEEE, 2014).

55. B. Cheng, J. M. Russell, W. Shi, L. Zhang, and E. T. Samulski, "Large-Scale, Solution-Phase Growth of Single-Crystalline SnO_2 Nanorods," *Journal of the American Chemical Society* 126 (2004): 5972–5973, https://doi.org/10.1021/ja0493244.

56. M. Loeza-Poot, R. Mis-Fernández, I. Rimmaudo, E. Camacho-Espinosa, and J. L. Peña, "Novel Sputtering Method to Obtain Wide Band Gap and Low Resistivity in As-Deposited Magnesium Doped Zinc Oxide Films," *Materials Science in Semiconductor Processing* 104 (2019): 104646, https://doi.org/10.1016/j.mssp.2019.104646.

57. L.-C. Yang, D.-R. Jung, F.-R. Po, C.-H. Hus, and J.-S. Fang, "Tailoring Bandgap and Electrical Properties of Magnesium-Doped Aluminum Zinc Oxide Films Deposited by Reactive Sputtering Using Metallic Mg and Al–Zn Targets," *Coatings* 10 (2020): 708, https://doi.org/10.3390/coatings10080708.

58. W. H. Baur, "Über die Verfeinerung der Kristallstrukturbestimmung Einiger Vertreter des Rutiltyps: TiO_2 SnO_2 GeO_2 und MgF_2," *Acta Crystallographica* 9 (1956): 515–520, https://doi.org/10.1107/S0365110X56001388.

59. W. Zachariasen, "The Crystal Structure of the Modification C of the Sesquioxides of the Rare Earth Metals, and of Indium and Thallium," *Norwegian Journal of Geology* 9 (1927): 310–316.

60. D. K. Smith and W. Newkirk, "The Crystal Structure of Baddeleyite (monoclinic ZrO_2) and Its Relation to the Polymorphism of ZrO_2," *Acta Crystallographica* 18 (1965): 983–991, https://doi.org/10.1107/S0365110X65002402.

61. K. R. Whittle, G. R. Lumpkin, and S. E. Ashbrook, "Neutron Diffraction and MAS NMR of Cesium Tungstate Defect Pyrochlores," *Journal of Solid State Chemistry* 179 (2006): 512–521, https://doi.org/10.1016/j.jssc.2005.11.011.

62. N. Nadaud, M. Nanot, J. Jové, and T. Roisnel, "A Structural Study of Tin-Doped Indium Oxide (ITO) Ceramics Using ^{119}Sn Mössbauer Spectroscopy and Neutron Diffraction," *Key Engineering Materials* 132–136 (1997): 1373–1376, https://doi.org/10.4028/www.scientific.net/KEM.132-136.1373.

63. N. Nadaud, N. Lequeux, M. Nanot, J. Jové, and T. Roisnel, "Structural Studies of Tin-Doped Indium Oxide (ITO) and $In_4Sn_3O_{12}$," *Journal of Solid State Chemistry* 135 (1998): 140–148, https://doi.org/10.1006/jssc.1997.7613.

64. A.-C. Dippel, O. Gutowski, L. Klemeyer, et al., "Evolution of Short-Range Order in Chemically and Physically Grown Thin Film Bilayer Structures for Electronic Applications," *Nanoscale* 12 (2020): 13103–13112, https://doi.org/10.1039/D0NR01847C.

65. G. King, J. R. Soliz, and W. O. Gordon, "Local Structure of $Zr(OH)_4$ and the Effect of Calcination Temperature From X-Ray Pair Distribution Function Analysis," *Inorganic Chemistry* 57 (2018): 2797–2803, https://doi.org/10.1021/acs.inorgchem.7b03137.

66. J. Krausmann, S. Sanctis, J. Engstler, M. Luysberg, M. Bruns, and J. J. Schneider, "Charge Transport in Low-Temperature Processed Thin-Film Transistors Based on Indium Oxide/Zinc Oxide Heterostructures," *ACS Applied Materials & Interfaces* 10 (2018): 20661–20671.

67. J. C. Hackley and T. Gougousi, "Properties of Atomic Layer Deposited HfO_2 Thin Films," *Thin Solid Films* 517 (2009): 6576–6583, https://doi.org/10.1016/j.tsf.2009.04.033.

68. D.-H. Son, D.-H. Kim, J.-H. Kim, et al., "Low Voltage, High Performance Thin Film Transistor with HfInZnO Channel and HfO_2 Gate Dielectric," *Electrochemical and Solid-State Letters* 13 (2010): H274, https://doi.org/10.1149/1.3428510.

69. L.-Y. Su, H.-Y. Lin, H.-K. Lin, S.-L. Wang, L.-H. Peng, and J. Huang, "Characterizations of Amorphous IGZO Thin-Film Transistors With Low Subthreshold Swing," *IEEE Electron Device Letters* 32 (2011): 1245–1247, https://doi.org/10.1109/LED.2011.2160931.

70. Y. J. Chung, J. H. Kim, U. K. Kim, M. Ryu, S. Y. Lee, and C. S. Hwang, "Study on the Existence of Abnormal Hysteresis in Hf-In-Zn-O Thin Film Transistors Under Illumination," *Electrochemical and Solid-State Letters* 14 (2011): H300, https://doi.org/10.1149/1.3589244.

71. W. L. Kalb and B. Batlogg, "Calculating the Trap Density of States in Organic Field-Effect Transistors From Experiment: A Comparison of Different Methods," *Physical Review B* 81 (2010), https://doi.org/10.1103/PhysRevB.81.035327.

72. J. Xie, K. Zhao, Q. Li, et al., "P-1.1: Co-Sputtering-Deposited Hf-Doped ITO Thin Films for Thin Film Transistors Application," *SID Symposium Digest of Technical Papers* 53 (2022): 572–574, https://doi.org/10.1002/sdtp.16027.

73. S. Zong, L. Xu, R. Liang, et al., "Enhance Electrical Performance and Stability of InSnMgO Thin-Film Transistors by Optimizing Carrier Concentration via Mg Doping," *IEEE Transactions on Electron Devices* 72 (2025): 277–281, https://doi.org/10.1109/ted.2024.3499949.

74. J.-I. Kim, K. H. Ji, M. Jang, H. Yang, R. Choi, and J. K. Jeong, "Ti-Doped Indium Tin Oxide Thin Films for Transparent Field-effect Transistors: Control of Charge-Carrier Density and Crystalline Structure," *ACS Applied Materials & Interfaces* 3 (2011): 2522–2528, https://doi.org/10.1021/am200388h.

75. W. Zeng, Z. Peng, D. Lin, A. A. Guliakova, Q. Zhang, and G. Zhu, "Tungsten-Doped Indium Tin Oxide Thin-Film Transistors for Dual-Mode Proximity Sensing Application," *ACS Applied Materials & Interfaces* 15 (2023): 52754–52766, https://doi.org/10.1021/acsami.3c11393.

76. M. Xu, S. Hu, L. Chen, X. Li, and J. Zhang, "Enhanced Illumination Stability of Solution-Processed Oxide Thin Film Transistor by Anion and Cation Co-Doping InSnO-Based Channel," *IEEE Electron Device Letters* 46 (2025): 1797–1800, https://doi.org/10.1109/led.2025.3598847.

77. Y. Wang, Z. Wang, K. Huang, et al., "Solution-Processed ITO Thin-Film Transistors With Doping of Gallium Oxide Show High On-Off Ratios and Work at 1 mV Drain Voltage," *Applied Physics Letters* 116 (2020): 141604, https://doi.org/10.1063/1.5141140.

78. Y. Chang, R. N. Bukke, Y. Kim, K. Ahn, J. Bae, and J. Jang, "High-Performance Amorphous InGaSnO Thin-Film Transistor with $ZrAlO_x$ Gate Insulator by Spray Pyrolysis," *Electronics* 12 (2023): 688, https://doi.org/10.3390/electronics12030688.

79. S.-N. Park, D.-H. Son, S.-J. Sung, J.-K. Kang, and D.-H. Kim, "Effects of Ta Addition Through Co-Sputtering on the Electrical Characteristics of Indium Tin Oxide Thin Film Transistors," *Journal of Nanoscience and Nanotechnology* 15 (2015): 386–390, https://doi.org/10.1166/jnn.2015.8341.

80. T. Kamiya, K. Nomura, and H. Hosono, "Origins of High Mobility and Low Operation Voltage of Amorphous Oxide TFTs: Electronic Structure, Electron Transport, Defects and Doping," *Journal of Display Technology* 5 (2009): 273–288, https://doi.org/10.1109/JDT.2009.2021582.

81. K. P. Kepp, "A Quantitative Scale of Oxophilicity and Thiophilicity," *Inorganic Chemistry* 55 (2016): 9461–9470, https://doi.org/10.1021/acs.inorgchem.6b01702.

82. T. Kamiya and H. Hosono, "Material Characteristics and Applications of Transparent Amorphous Oxide Semiconductors," *NPG Asia Materials* 2 (2010): 15–22.

83. S. Lee, K. Ghaffarzadeh, A. Nathan, et al., "Trap-Limited and Percolation Conduction Mechanisms in Amorphous Oxide Semiconductor Thin Film Transistors," *Applied Physics Letters* 98 (2011): 203508.

84. M. Januar, C.-W. Cheng, W.-K. Lin, et al., "Correlating the Density of Trap-States and the Field-Effect Performance in Metal-Oxide Thin-Film Transistors with High-$\Kappa$ Gate Dielectrics via a Trap-Limited Conduction Method," *IEEE Transactions on Nanotechnology* 20 (2021): 321–331, https://doi.org/10.1109/TNANO.2021.3058408.

85. M. Ghittorelli, F. Torricelli, L. Colalongo, and Z. M. Kovacs-Vajna, "Accurate Analytical Physical Modeling of Amorphous InGaZnO Thin-Film Transistors Accounting for Trapped and Free Charges," *IEEE Transactions on Electron Devices* 61 (2014): 4105–4112, https://doi.org/10.1109/ted.2014.2361062.

86. K. Jones and M. F. Lappert, "Amino Derivatives of Metals and Metalloids," *Journal of Organometallic Chemistry* 3 (1965): 295–307.

87. G. M. Diamond, R. F. Jordan, and J. L. Petersen, "Efficient Synthesis of Chiral Ansa -Metallocenes by Amine Elimination. Synthesis, Structure, and Reactivity of Rac -(EBI)Zr(NMe_2)$_2$," *Journal of the American Chemical Society* 118 (1996): 8024–8033, https://doi.org/10.1021/ja9604830.

88. G. M. Diamond, R. F. Jordan, and J. L. Petersen, "Synthesis of Group 4 Metal Rac -(EBI)M(NR_2)$_2$ Complexes by Amine Elimination. Scope and Limitations," *Organometallics* 15 (1996): 4030–4037, https://doi.org/10.1021/om960103j.

89. M. Luysberg, M. Heggen, and K. Tillmann, "FEI Tecnai G2 F20," *Journal of Large-Scale Research Facilities JLSRF* 2 (2016): A77.

90. M. Kruth, D. Meertens, and K. Tillmann, "Fei Helios Nanolab 460F1 FIB-SEM," *Journal of Large-Scale Research Facilities* 2 (2016): A59.

91. J. H. Scofield, "Hartree-Slater Subshell Photoionization Cross-Sections at 1254 and 1487 eV," *Journal of Electron Spectroscopy and Related Phenomena* 8 (1976): 129–137.

92. M. Zimmermann, O. Ivashko, F. Igoa Saldaña, et al., "P21.1 at PETRA III – A High-Energy X-Ray Diffraction Beamline for Physics and Chemistry," *Journal of Synchrotron Radiation* 32 (2025): 802–814, https://doi.org/10.1107/S1600577525002826.

93. J. Kieffer and J. P. Wright, "PyFAI: A Python Library for High Performance Azimuthal Integration on GPU," *Powder Diffraction* 28 (2013): S339–S350, https://doi.org/10.1017/s0885715613000924.

94. P. Juhás, T. Davis, C. L. Farrow, and S. J. L. Billinge, "PDFgetX3: A Rapid and Highly Automatable Program for Processing Powder Diffraction Data Into Total Scattering Pair Distribution Functions," *Journal of Applied Crystallography* 46 (2013): 560–566, https://doi.org/10.1107/S0021889813005190.

95. X. Yang, P. Juhás, C. L. Farrow, and S. J. L. Billinge, "xPDFsuite: An End-to-End Software Solution for High Throughput Pair Distribution Function Transformation, Visualization and Analysis," *arXiv* (2014): 1402.3163.

96. Fraunhofer IPMS, End-of-Line Standard Substrates for the Characterization of Organic Semiconductor Materials: OFET-Structures on Silicon With Au Source/Drain and 90 Nm SiO_2 Gate-Insulator Generation 4, http://www.ipms.fraunhofer.de/.

97. NanoBioAnalytics, UV-Ozon-Reiniger UVC-1014, (accessed 2025), http://www.nanobioanalytics.com/UVC-1014.php.

Supporting Information

Additional supporting information can be found online in the Supporting Information section.

Supporting File: aelm70294-sup-0001-SuppMat.docx.